Available online at www.sciencedirect.com

ScienceDirect

Advances in Space Research xxx (xxxx) xxx

ADVANCES IN SPACE RESEARCH (a COSPAR publication)

www.elsevier.com/locate/asr

Effects of planetary wave oscillation on E-sporadic (*Es*) layers during the rare Antarctic sudden stratospheric warming of 2019 ☆

Pedro A. Fontes [a,b,*], Marcio T.A.H. Muella [b,**], Laysa C.A. Resende [c,d], Rodolfo de Jesus [c,d], Paulo R. Fagundes [b], Gourav Mitra [e], Valdir G. Pillat [b], Paulo P. Batista [d], Ricardo A. Buriti [f], Emília Correia [d,g], Peter T. Muka [b,h]

[a] *Department of Research and Innovation, Instituto Federal do Maranhão, Alcântara, MA 65250-000, Brazil*
[b] *Institute of Research and Development, Universidade do Vale do Paraíba, São José dos Campos, SP 12244-000, Brazil*
[c] *State Key Laboratory of Space Weather, Beijing 100190, China*
[d] *Aeronomy Division, Instituto Nacional de Pesquisas Espaciais, São José dos Campos, SP 12227-010, Brazil*
[e] *Space and Atmospheric Sciences Division, Physical Research Laboratory, Ahmedabad, GJ 380009, India*
[f] *Department of Physics, Universidade Federal de Campina Grande, Campina Grande, PB 58429-900, Brazil*
[g] *School of Engineering, CRAAM, Universidade Presbiteriana Mackenzie, São Paulo, SP 01302-907, Brazil*
[h] *Department of Pure and Applied Physics, Ladoke Akintola University of Technology, Ogbomoso, Oyo-State 4000, Nigeria*

Received 28 November 2024; received in revised form 24 April 2025; accepted 26 April 2025

Abstract

This study investigates the impact of the rare 2019 Antarctic Sudden Stratospheric Warming (SSW) event on the top frequency parameter (*ftEs*) of the sporadic E (*Es*) layers, using data from several ionosondes located at low and mid-latitudes across the Southern and Northern Hemispheres, including stations in the American, Oceanian, and Asian regions. The ionosonde data were also used to identify frequency anomalies in the *Es* layers during the event. Additionally, data from three meteor radars in South America were used to further analyze the impact of the SSW, focusing on key parameters such as tidal winds and Planetary Wave (PW) oscillations. The study found significant *ftEs* peaks *exceeding* 10 MHz, particularly at low-latitude stations, with values reaching up to 20 MHz. The presence of these atypical peaks in *ftEs* was related to PW activity, which intensified the electron densities in the *Es* layers. A wavelet analysis of the *ftEs* and neutral wind data revealed oscillations associated with PW and tidal interactions, with dominant periods of ~2–8-days. These patterns were more pronounced in the Southern Hemisphere, indicating stronger PW-tide coupling compared to the Northern Hemisphere. In addition, this study shows that the non-linear interaction between the PW and the tides occurred globally, generating secondary oscillations of ~2–8-days on the *Es* layer development for the three continents. These oscillations were observed in the zonal (U) and meridional (V) winds of the diurnal and semidiurnal tides (DT and ST) during the SSW event, demonstrating a coupling in the troposphere-stratosphere-lower atmosphere dynamics. The coupling between the stratosphere and lower thermosphere contributed to the observed anomalies, revealing the broader impacts of SSW events on *Es* layer behavior. This study provides an understanding of

☆ This article is part of a special issue entitled: 'Ionospheric Imaging' published in Advances in Space Research.

* Corresponding authors at: Department of Research and Innovation, Instituto Federal do Maranhão, Alcântara, MA 65250-000, Brazil.
** Corresponding author.
E-mail addresses: pedro.fontes@ifma.edu.br (P.A. Fontes), mmuella@univap.br (M.T.A.H. Muella).

https://doi.org/10.1016/j.asr.2025.04.069

0273-1177/© 2025 COSPAR. Published by Elsevier B.V. All rights are reserved, including those for text and data mining, AI training, and similar technologies.

Please cite this article as: P. A. Fontes, M. T. A. H. Muella, L. C. A. Resende et al., Effects of planetary wave oscillation on E-sporadic (*Es*) layers during the rare Antarctic sudden stratospheric warming of 2019, Advances in Space Research, https://doi.org/10.1016/j.asr.2025.04.069

the impact of SSW on *Es* layers, using ionosonde data and wave oscillation analysis that could enhance data assimilation models for more accurate ionospheric prediction.
© 2025 COSPAR. Published by Elsevier B.V. All rights are reserved, including those for text and data mining, AI training, and similar technologies.

Keywords: Sporadic-E layer; Sudden stratospheric warming; Planetary wave; Tidal winds

1. Introduction

The *Es* layers consist of densities of metallic ions, which originate primarily from meteoric ablation, as well as molecular ions. They are formed at low and mid-latitudes by the wind shear mechanism, at altitudes between approximately 100 and 140 km in the E region of the ionosphere (Whitehead, 1989; Mathews, 1998; Chu et al., 2014; Resende et al., 2018; Bergsson and Syndergaard, 2022; Fontes et al., 2023). Wind shear occurs when the meridional (north–south) or zonal (east–west) wind components move in opposite directions, leading ions to drift toward a point (ion convergence) where the wind speed is zero (Pancheva et al., 2003; Haldoupis et al., 2007; Chu et al., 2014; Andoh et al., 2020; Tang et al., 2022). At this point, the ions accumulate, and the electrons follow the magnetic field lines to maintain the plasma neutrality, significantly increasing the density in the region and leading to the formation of the *Es* layers.

Sudden Stratospheric Warming (SSW) is a global phenomenon that occurs in the winter stratosphere, characterized by a sudden increase in polar temperatures over a period of several days (Matsuno, 1971). These events can be caused when large Planetary Waves (PWs) "break" both horizontally and vertically, releasing a large amount of energy (Yamazaki et al., 2020). The PW from the troposphere vertically interacts with the stratosphere, then a significant amount of energy is released upward at high latitudes during winter, which can slow down or even reverse the polar vortex circulation, resulting in SSW (Yamazaki et al., 2020; Mitra et al., 2023). During an SSW event, the stratopause descends, causing a sudden warming of the stratosphere and cooling of the mesosphere. As a result, the slowing or reversal of the zonal winds cannot keep up with the warming (Matsuno, 1971; Wang et al., 2011; Chau et al., 2012; Choi et al, 2019; Ma et al., 2020; Zhang et al., 2021).

SSWs are rare in the Southern Hemisphere (SH) and common in the Northern Hemisphere (NH) (Krüger et al, 2005; Charlton and Polvani, 2007; Goncharenko et al., 2020). According to previous works, the rarity of SSWs in the SH is attributed to its weaker land-sea contrast and the smaller amplitudes of PWs present in this region (Krüger et al., 2005; Ren and Cai, 2008; Rao and Ren, 2020; Rao et al., 2020). The 2019 SSW event, which is the main focus of this study, has been demonstrated to exhibit a more rapid and significant temperature increase than the 2002 event, the last SSW observed in the SH with a zonal wind inversion (Rao et al., 2020; Eswaraiah et al., 2020). Yamazaki et al. (2020) suggested that this 2019 event in the SH occurred due to the disruption of the zonal wavenumber one PW in the polar stratosphere between ~30 and 40 km height. In other words, it was generated by the strong vertical wind shear associated with the breaking of the PW. More specifically, Mitra et al. (2022) demonstrated the salient role of stationary planetary wave zonal wavenumber 1 in preconditioning the 2019 event. PWs can interact with the atmospheric tides, generating two secondary oscillations with frequencies corresponding to the sum and difference of the primary wave frequencies (Forbes et al., 2020). For this reason, PW oscillations can be observed in phenomena occurring in the lower thermosphere, well above where these oscillations typically originate (Fontes et al., 2024).

The impact of SSW events on atmospheric phenomena has been investigated by several authors (Lima et al., 2012; Chau et al., 2012; Fagundes et al., 2015; Jesus et al., 2017; Li et al., 2020; Lin et al., 2020; Zhang et al., 2021; Ma et al., 2022; Mitra et al., 2023; Fontes et al., 2024). Lima et al. (2012) observed that North Hemisphere SSW has affected tides and 2-days PW on equatorial region. Chau et al. (2012) found significant changes in total electron content (TEC) and electron density profiles associated with modifications in the equatorial zonal electric fields during the 2008 and 2009 SSW events in the NH. Fagundes et al. (2015) reported a significant ionospheric disturbance at low and equatorial latitudes in the SH, which persisted for 5 to 6-days in response to the 2009 SSW event. Lin et al. (2020) have shown that the variability of the amplitude of the quasi-6-days waves (Q6DW) indicates a possible effect related to two secondary waves through the Q6DW-tide interaction during the 2019 SSW event, with a peak between ±20° around 12 LT. Ma et al. (2022) proposed that the mechanism of global Q6DWs is enhanced during SSWs, with interhemispheric propagation amplifying Q6DWs specifically during the 2019 SSW event. Mitra et al. (2023) observed consistent variability in the tidal components DW1 (diurnal westward tide with zonal wavenumber 1), DE3 (diurnal eastward tide with zonal wavenumber 3), and SW2 (semidiurnal westward tide with zonal wavenumber 2) in response to the 2019 SSW event in the SH. More recently, Fontes et al. (2024) showed from ionosonde measurements atypical sporadic-E (*Es*) layer frequency peaks during SSW events, which were attributed

to the non-linear interaction between PWs and primary atmospheric tides at low latitudes in the SH.

PWs can influence *Es* layers in various ways. One of the primary mechanisms is the modulation of neutral winds at E-region altitudes, which modifies the wind shear and, consequently, the ion convergence responsible for *Es* layer formation. PWs affect the transport of metallic ions in the E region, leading to their accumulation at specific altitudes and contributing to the development of intense *Es* layers. Additionally, PWs interact non-linearly with atmospheric tides, a process that can amplify or modify tidal wind patterns, further affecting *Es* layer variability. During SSW events, these non-linear interactions generate secondary waves with periods ranging from 2 to 8 days. These secondary waves propagate into the lower thermosphere, where they influence wind shear, leading to variations in the intensity and altitude of *Es* layers. For instance, an increase in wind shear can result in strong *Es* layers with high electron densities. Studies based on ionosonde data, meteor radars, and satellite observations have demonstrated that PWs exert significant global and seasonal effects during SSW events (Teitelbaum and Vial, 1991; Haldoupis and Pancheva, 2002; Korenkova et al., 2015; Gu et al., 2016; Forbes et al., 2020; Miyoshi and Yamazaki, 2020; Yamazaki et al., 2020; Ma et al., 2022).

In view of the above, this study aims to investigate the effects of the rare Antarctic SSW event of 2019 on the *Es* layers observed at low and mid latitudes. To do this, we used the *ftEs* parameter obtained from digisondes located in both hemispheres of the American, Oceanian, and Asian continents. In addition, neutral wind data from meteor radars located on the American continent in the SH were used. Moreover, it is worthwhile mentioning that data assimilation has become a crucial technique in space weather sciences, allowing for the integration of observational data into models. In this context, understanding the effects of SSW on *Es* layers provides valuable input for data assimilation systems. By analyzing ionosonde data and wave oscillations, this study contributes to a better understanding of the spatiotemporal variability of *Es* layers during SSW events. The findings of this work are essential for refining data assimilation models, as they allow for more accurate predictions of ionospheric behavior, particularly under extreme stratospheric conditions. The following section outlines the methodology and data analysis employed in this work. Then, Section 3 presents the results obtained and includes the discussion. Finally, Section 4 summarizes the main conclusion of this present study.

2. Methodology and data analysis

2.1. Stratospheric and geomagnetic data

For the SSW event that occurred in the SH in 2019, we used data collected between August 1 and October 31, 2019. The data analysis employed stratospheric temperature at 10 hPa (~30 km) at high latitude (90°S) in the SH, zonal wind data at 10 hPa at 60°S, and planetary wave data with zonal wavenumbers 1 (PW1) and 2 (PW2) at 10 hPa at 60°S. These data were obtained from the NASA online data service (https://acd-ext.gsfc.nasa.gov/Data_services/met/ann_data.html). Daily values of the geomagnetic indices Dst and Ap were obtained from the World Data Center for Geomagnetism (WDC), Kyoto (https://wdc.kugi.kyoto-u.ac.jp/wdc/Sec3.html). The geomagnetic indices are used to show the presence or absence of geomagnetic storms during the SSW event (Korenkov et al., 2012; Giday et al., 2016; Matzka et al., 2021).

2.2. Es layer database

The *Es* layer parameter used in this study was obtained online from the Lowell GIRO Data Center (LGDC), which provides global Digisonde (Table 1 and Fig. 1) data in cooperation with several countries (https://giro.uml.edu/didbase/scaled.php). The Digisondes at the LGDC are high-frequency radars that transmit waves in the range of 1−30 MHz, with a frequency step of 0.05 MHz. These Digisonde systems are capable of detecting signals reflected from the ionosphere at altitudes ranging from 100 to 1200 km, with temporal resolutions of 5, 10, and 15 min to monitor ionospheric variations (Reinisch et al., 2009). In addition to the LGDC stations, data from three CADI (Canadian Advanced Digital Ionosonde) ionosondes installed in the Brazilian longitudinal sector were used in the analysis. The CADI observatories are located at Araguatins (ARA, 5.65°S; 48.12°W), Jataí (JAT, 17.88°S; 51.72°W), and São José dos Campos (SJC, 23.18°S; 45.89°W). The CADI system registered reflected signal echoes from 1 to 20 MHz with temporal resolution of 5 min (Huang and MacDougall, 2005). The ionograms recorded by the CADI system were processed with the computer software UDIDA (Univap Digital Ionosonde Data Analysis), which was also used to visualize and manually scale the *Es* layer parameter (Pillat et al., 2013).

Table 1 lists the names of the 12 digital ionosonde observatories used in this study, including their abbreviation codes, geographic coordinates, and dip latitudes. It is clearly noted that the digital ionosonde stations are distributed between the mid- and low latitudes of the SH (American and Oceanian continents) and NH (American and Asian continents), as also shown in the map in Fig. 1. The selected ionosondes have observation intervals of 5 and 15 min, and the parameter of top frequency of the *Es* layers (*ftEs*) were scaled from the ionograms recorded at these intervals.

The *ftEs* refers to the *foEs* (critical frequency of the *Es* layer) in the digital ionosonde data and corresponds to the highest frequency of the *Es* trace when the ordinary and extraordinary echoes cannot be distinguished. This frequency is proportional to the electron density of the *Es* layer, and for any practical purpose can be used as representative of its variability (Fontes et al., 2023).

Table 1
Location of the digital ionosonde stations.

Digital Ionosondes					
	Station	Continent	Code	Geog. Coordinates	Dip Latitude
1	Jeju	Asian	JEJ	33.43°N; 126.3°E	27.26°
2	Austin	American	AUS	30.4°N; 97.74°W	39.60°
3	Lualualei	American	LUA	21.43°N; 158.16°W	21.07°
4	Ramey	American	RAM	18.5°N; 64.14°W	25.25°
5	Araguatins	American	ARA	5.65°S; 48.12°W	–4.92°
6	Cocos Islands	Oceanian	COI	12.18°S; 96.84°E	–21.62°
7	Darwin	Oceanian	DAR	12.45°S; 130.84°E	–21.23°
8	Jataí	American	JAT	17.88°S; 51.72°W	–13.23°
9	Niue	Oceanian	NIU	19.07°S; 169.92°E	–24.59°
10	São José dos Campos	American	SJC	23.18°S; 45.89°W	–20.23°
11	Brisbane	Oceanian	BRI	27.06°S; 153.06°E	–35.71°
12	Canberra	Oceanian	CAN	35.32°S; 149.15°E	–45.03°

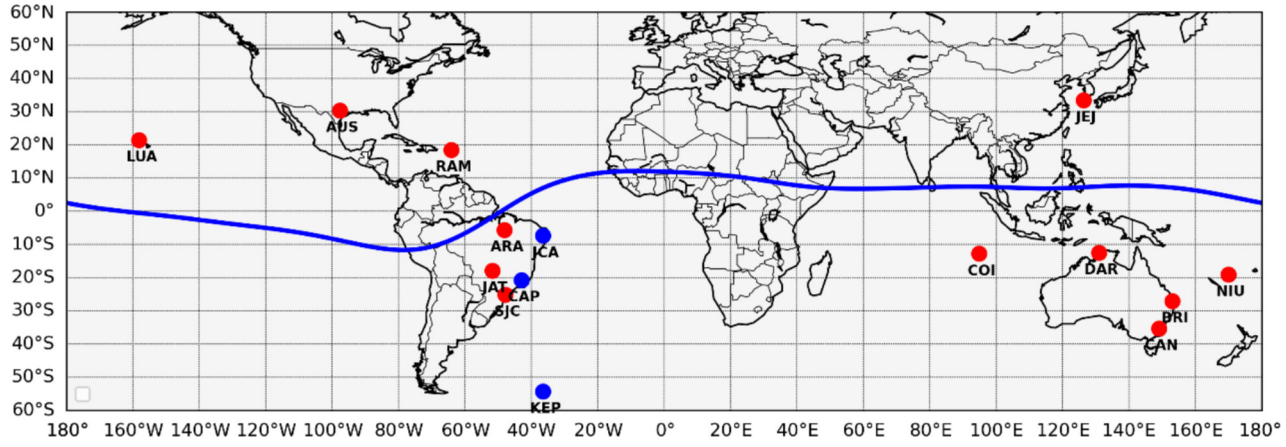

Fig. 1. Map showing the location of the digital ionosondes (red dots) and meteor radars (blue dots) at mid- and low latitudes in the Southern (American and Oceanian continents) and Northern (American and Asian continents) Hemispheres. The blue line is the magnetic equator.

Table 2
Location of the meteor radar stations.

Meteor Radars					
	Station	Continent	Code	Geog. Coordinates	Dip Latitude
1	São João do Cariri	American	JCA	7.4°S; 36.5°W	–12.5°
2	Cachoeira Paulista	American	CAP	22.7°S; 45°W	–20.3°
3	King Edward Point	American	KEP	54.3°S; 36.5°W	–45.6°

2.3. Meteor radar database

The zonal and meridional wind data used in this work were obtained from the SkiYMET meteor radars installed at the observatories of King Edward Point (KEP, 54.3°S; 36.5°W), Cachoeira Paulista (CAP, 22.7°S; 45°W), and São João do Cariri (JCA, 7.4°S; 36.5°W). The coordinates and location of these radars are also listed in Table 2 and shown as blue dots in Fig. 1.

Meteor radar systems measure horizontal wind values at an altitude range of 80–100 km, with a vertical resolution of 3 km and a temporal resolution of 1 h (Hocking, 2004; Buriti et al., 2008; Andrioli et al., 2009). JCA and CAP radars operate at 35.24 MHz frequency, 2144 pulses.s^{-1} repetition frequency and 12 kW peak power. The radar at KEP operates at 32.5 MHz frequency, 2144 pulses.s^{-1} rate, and 6 kW peak power (Mitra et al., 2023). Meteor radar data from the KEP, CAP, and JCA

stations were used to perform a wavelet power spectrum analysis to determine if PW oscillations were present in the neutral wind data.

2.4. Merra-2 database

MERRA-2 (Modern-Era Retrospective analysis for Research and Applications version 2) is the latest version of NASA's global atmospheric satellite reanalysis, developed by the Global Modeling and Assimilation Office (GMAO) using the Godard Earth Observing System (GEOS) model (Gelaro et al., 2017). Data is available from 1980 to the present. This work used zonal wind data in the ~0.01 hPa range (~75 km) with a latitude-longitude grid of 0.5° × 0.625°. In addition to wind data, we used water vapor (H_2O) and total column ozone (O_3) data for the latitudes of KEP, CAP, and JCA. Zonal wind data can be obtained from the website: https://disc.gsfc.nasa.gov/datasets/M2I1NXASM_5.12.4/summary.

2.5. Metop-B database

The Infrared Atmospheric Sounding Interferometer (IASI) is a high-resolution spectrometer that has been operating on board the Metop-A, Metop-B, and Metop-C satellites of EUMETSAT (European Organization for the Exploitation of Meteorological Satellites) since 2006, 2012, and 2018, respectively. Ozone (O_3) data were retrieved from Metop-B due to its better data quality for the period studied, specifically within the spectral bands of 1.025–1.075 cm^{-1}. The IASI-Metop-B ozone data are consistent with observations in the Antarctic region during the study period, showing differences of less than 1 % for O_3. The Metop-B data are available on the website: https://iasi.aeris-data.fr/o3/.

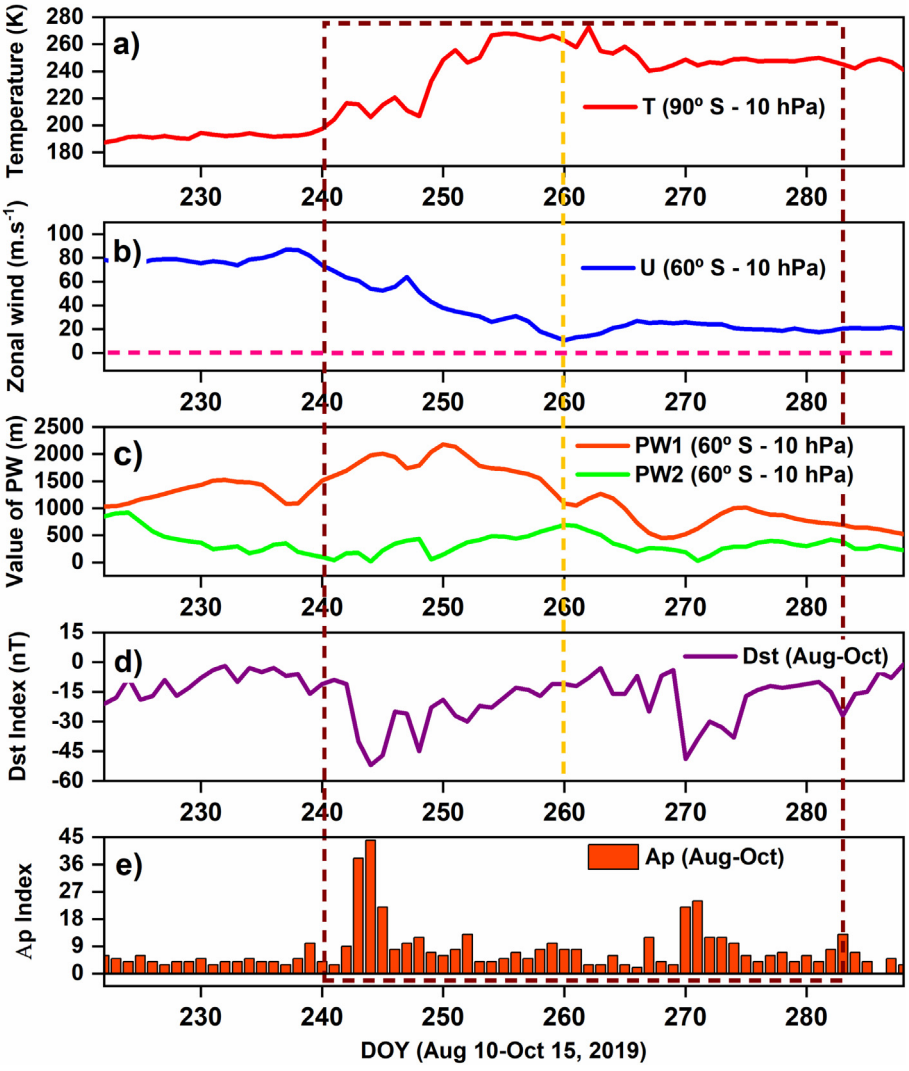

Fig. 2. Data from the September 2019 SSW event at high latitudes in the SH: (a) temperature at 90° S at 10 hPa (~30 km), (b) zonal wind at 10 hPa (The pink horizontal line corresponds to zero wind), (c) PW1 and PW2 wave value at 10 hPa, (d) Dst index, and (e) Ap index. The rectangle with brown dashed lines indicates the days of the 2019 SSW event in the SH. The vertical yellow line corresponds to the central day (DOY 260, September 17) of the Antarctic SSW in 2019.

3. Results and discussion

The rare Antarctic SSW of 2019 had a sudden temperature rise. However, the reverse of the zonal wind at 60°S at 10 hPa (~30 km) did not occur. Therefore, the 2019 SSW is considered a weak event (Rao et al., 2018; Xie et al., 2020; Statnaia et al., 2020).

3.1. Temperature, zonal wind, planetary waves, and geomagnetic indices

Fig. 2 shows that the 2019 Antarctic SSW began in late August and lasted until early October (brown dotted rectangle). This figure shows data for 2019 from DOY 222 (August 10) to DOY 288 (October 15). Fig. 2a shows the result of the sudden temperature increase at high latitude (90°S), where the pressure is 10 hPa (~30 km altitude). The temperature begins to rise on DOY 240 (August 28, ~197 K) and peaks on DOY 262 (September 19, ~272 K). The results are consistent with Liu et al. (2022), who showed that the temperature around the pole begins to increase between DOYs 240–242 (between August 28 and 30), and between DOYs 243–245 (between August 31 and September 2), the high temperature region becomes larger while the low temperature region moves away from the South Pole, and then the temperature peaks on DOY 254 (September 11) with a weakening of the polar vortex. The zonal wind starts to slow down one day before the temperature increases, starting on DOY 239 (August 27, ~82 m s^{-1}), and reaches its lowest speed on DOY 260 (September 17) with ~10 m s^{-1} (Fig. 2b). The pink line in Fig. 2b shows that there was no reversal of the zonal wind. Thus, DOY 260 (September 17) was considered to be the peak of the 2019 Antarctic SSW in the SH since the zonal wind reached its lowest speed (Eswaraiah et al., 2020; Mitra et al., 2023).

It is possible to observe that both the temperature and the zonal wind remain approximately constant from DOY 267 (September 24) to DOY 283 (October 10, at ~240 K and ~25 m s^{-1}, respectively). Eswaraiah et al. (2020) compared the Antarctic SSW events of 2002 (an event in the SH with zonal wind reversal) and 2019 (an event in the SH without zonal wind reversal) and found that the variation in temperature (Fig. 2a) and zonal wind (Fig. 2b) was greater in 2019 (~68 K and 72 m s^{-1}) than in 2002 (~50 K and 66 m s^{-1}). Mitra and Guharay (2024) also compared these two events and determined the impact of the 2019 SSW by isolating the seasonal contribution, which occurs at the same time interval. This is important because the SSW event in the SH occurred around the vernal equinox. Noguchi et al. (2020) proposed that a significant increase in convective activity in the NH tropics occurred in response to the 2019 Antarctic SSW. The authors attribute this to a response due to the change in the basic state of the stratosphere during the advanced phase of cooling of the lower stratosphere by the enhanced Brewer-Dobson circulation through the Antarctic SSWs, and probably significantly slowed the zonal wind at 60°S and 10 hPa (~30 km altitude).

The values of the PWs are shown in Fig. 2c, where the dominant wave throughout the event was PW1 (planetary wave with zonal wavenumber 1). At the beginning of the event, PW1 had a value of ~1513 m (DOY 240) and reached the maximum value of the event at ~2180 m on DOY 250 (September 7), 10 days before the considered peak of the 2019 Antarctic SSW (DOY 240), but in close time association with day the temperature reached the higher level. After this point, PW1 began to decrease in value, reaching ~1092 m at the peak of the SSW, continuing to decrease in value reaching the low level of ~453 m on DOY 268 (September 25). On the other hand, PW2 (planetary wave with zonal wavenumber 2) showed much smaller value variations throughout the Antarctic SSW in 2019, reaching a maximum of ~691 m at the peak of the event (DOY 240). The dominance of PW1 during the entire duration of an SSW indicates that the event was of the displacement type (D), which can contribute to the Brewer-Dobson circulation (Choi et al., 2019; Ma et al., 2020).

Fig. 2d and 2e show the geomagnetic indices Dst and Ap, respectively, which are used to verify whether any geomagnetic storms occurred during the Antarctic SSW period of 2019. It can be observed that a weak geomagnetic storm took place shortly after the onset of the event but well before the central day on DOY 260 (September 17). The lowest daily Dst value reached approximately −52 nT, and the daily Ap index attained ~44 on DOY 244 (September 1) (Matzka et al., 2021). After the central day of the SSW event, another weak geomagnetic storm occurred on DOY 270 (September 27), with the Dst values reaching approximately −49 nT and the Ap index reaching ~24.

3.2. Behavior of Es layers and PW during the 2019 Antarctic SSW in the SH and NH

Sudden increases in the *ftEs* with peak values above ~10 MHz can be considered atypical for layers formed by tidal winds. In fact, these frequencies usually reach a maximum of ~7 MHz (Maksyutin et al., 2001; Maksyutin and Sherstyukov, 2005; Korenkova et al., 2015). Fig. 3 shows an ionogram from the ARA station on DOY 257 (22:50 UT) where an atypical flat-type *Es* layer was observed with an *ftEs* peak at 20 MHz. The fact that this Es_f-type layer blocks the F-layer and occurs at night indicates that it is an *Es* layer formed by tidal winds.

Fig. 4 shows the *ftEs* values (in MHz) observed at the low latitude stations in the SH of the American continent (SJC, JAT, and ARA), in which the presence of large peaks with values above ~10 MHz were clearly observed at the station located closer to the magnetic equator (ARA). Fig. 4a shows the results of the *ftEs* for the SJC station, with the highest peak at ~12 MHz (~13 UT and ~03 UT) at the end of the 2019 Antarctic SSW event. Similarly to SJC, for the JAT station (Fig. 4b) the highest peak

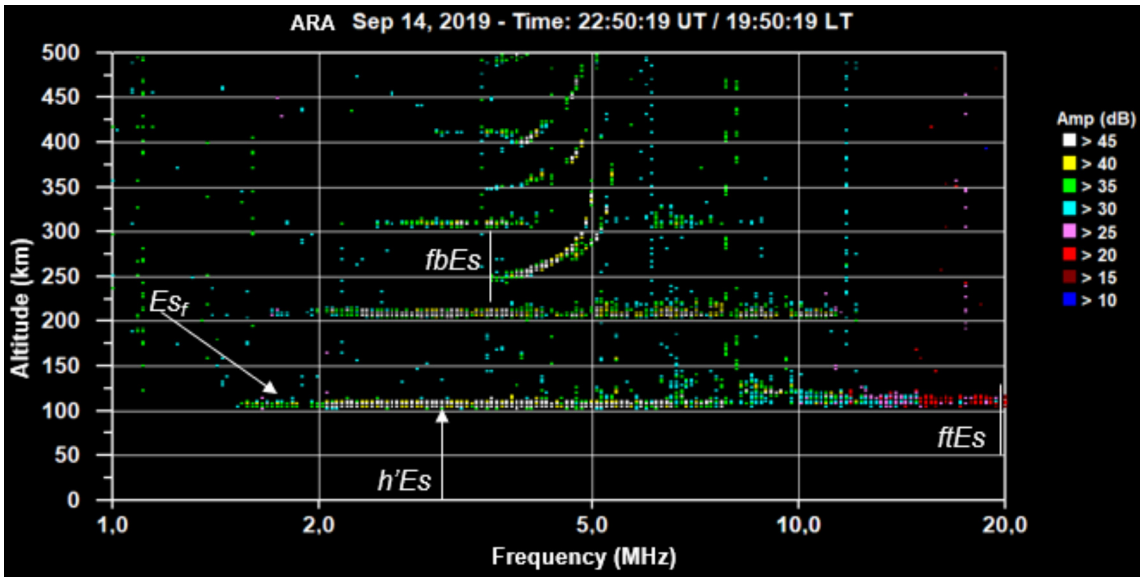

Fig. 3. Ionogram showing an atypical Es layer with a ftEs peak at 20 MHz. Es_f is the flat-type Es layer, ftEs is the top frequency of the Es layer, fbEs is the blanketing frequency of the Es layer, and h'Es is the virtual height of the Es layer.

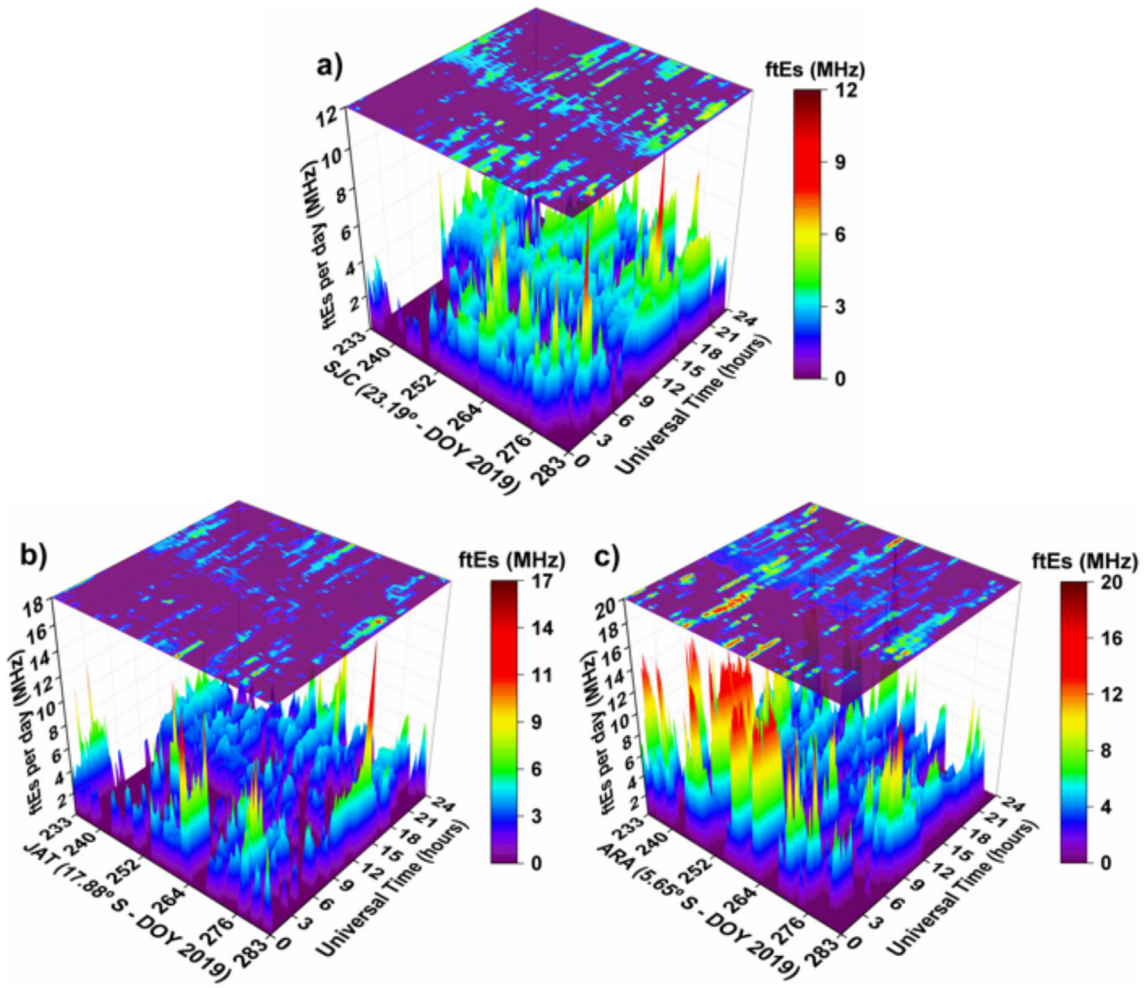

Fig. 4. 3D plots of the daily and temporal variability of the ftEs observed at low latitude stations (a) SJC, (b) JAT, and (c) ARA, located in the SH of the American continent, during the 2019 Antarctic SSW event. The ftEs values were colored according to the scale shown on the bars, with the highest value in the range being the maximum peak in ftEs observed at that station.

values of *ftEs* (~17 MHz at 14:30 UT) were observed at the end of the SSW event. However, the results from this station also showed *ftEs* of ~10 MHz throughout the SSW event, including a peak of ~14 MHz in the early hours (~00:30 UT) of DOY 263. For the station of ARA, Fig. 4c shows that *ftEs* presented high values above ~14 MHz between DOYs 233–263 (from 01 to 07 UT) and reached a peak value of 20 MHz on DOY 257 (~23 UT).

Haldoupis and Pancheva (2006) analyzed the atypical enhancements on the frequency parameters of the *Es* layers, and found a long-term periodicity, which they attributed to the action of PWs. Planetary waves can be a secondary mechanism in the formation of *Es* layers that can modify and intensify the electron densities of the region and their associated values of *ftEs* (Haldoupis and Pancheva, 2002; Pancheva et al., 2003; Haldoupis et al., 2004). PW oscillations originate in the troposphere and reach the lower thermosphere through non-linear interaction with the tidal winds. The theory suggests that metal ions are trapped in large vortices by PWs and can enhance the frequencies of the *Es* layers (Shalimov et al., 1999; Voiculescu et al., 2000; Shalimov and Haldoupis, 2002; Haldoupis and Pancheva, 2002; Pancheva et al., 2003; Haldoupis et al., 2004). According to Gu et al. (2018), the non-linear interaction between PW and tides may form secondary waves with zonal wavenumbers and frequencies equal to the sum and difference of the main waves. This probably explains why PW waves generated in the troposphere (up to ~12 km) show their oscillations in the stratosphere (up to ~50 km) and lower thermosphere (between ~90 and 120 km), where the *Es* layers are formed. Fontes et al. (2024) investigated the effect of three major SSW events in the NH (Feb/2018, Dec/2018–Jan/2019, and Dec/2020–Jan/2021) on the *Es* layers in the SH. They found that there was an intensification of the *ftEs* values with atypical peaks of ~20 MHz, and oscillations characteristics associated with PWs. The authors argued that this enhancement of the *ftEs* peaks is due to the accumulation of metal ions at heights where the *Es* layers are formed, caused by the non-linear interaction between the PW and the tides.

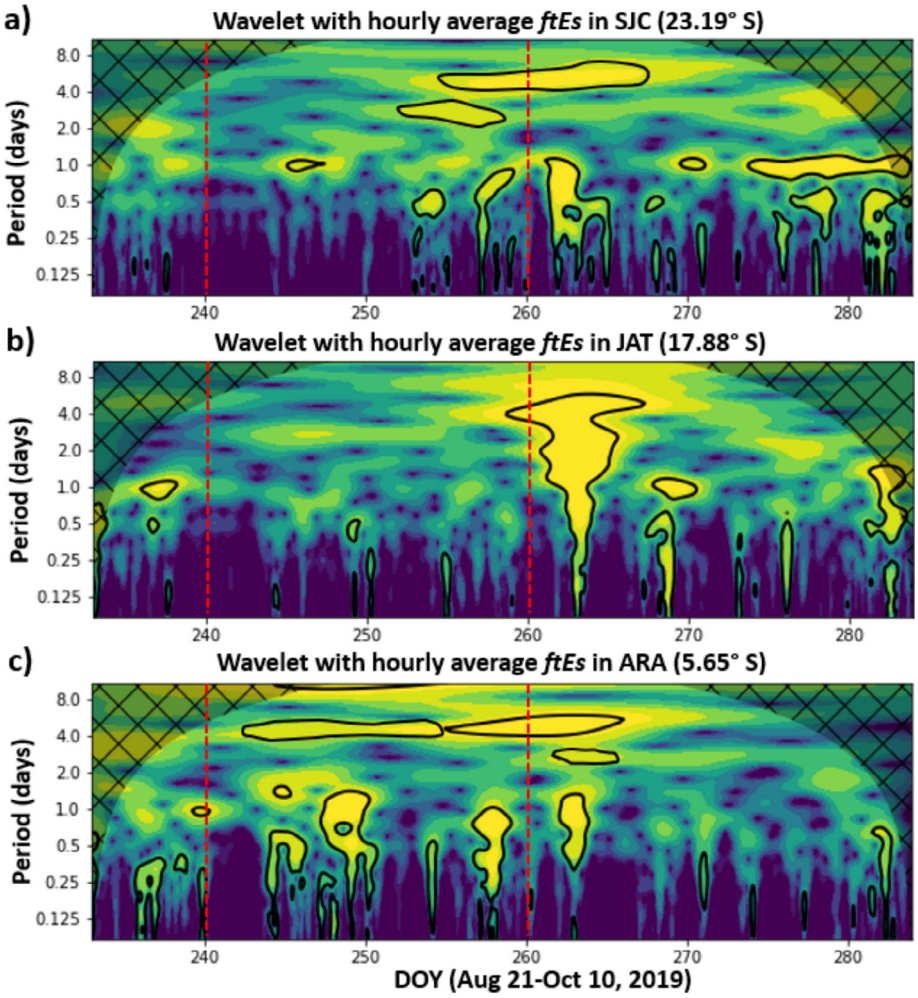

Fig. 5. Wavelet power spectrum analysis of the ftEs parameter during the 2019 Antarctic SSW event at: (a) SJC, (b) JAT, and (c) ARA. The first vertical dashed line in red corresponds to the start of the event (DOY 240), and the second line corresponds to the central day of the event (DOY 260). The wavelet has been normalized to a 95% confidence level, with the black contour lines representing the significant spectral peaks.

Fig. 5 shows the characteristics of the PW oscillations observed during the 2019 Antarctic SSW event at the low latitude stations located in the SH of the American continent. The panels (a–c) of Fig. 5 shows the wavelet power spectrum analyses of the *ftEs* parameter obtained in SJC, JAT, and ARA. For example, in Fig. 5a for the SJC station, it is possible to notice that in addition to the primary waves associated with the diurnal (24 h) and semidiurnal (12 h) tidal oscillations, there are periodicities of ~3–6-days starting from DOY 252 until DOY 268. It means that the PW oscillations are occurring throughout the central day of the SSW event on DOY 260. These PW oscillations are also present in the wavelet analysis of the *ftEs* at JAT, as shown in Fig. 5b. At this station, oscillations of ~2–6-days are observed from DOYs 258–268. Fig. 5c shows that at the station of ARA, PW oscillations with ~4–6-days are observed from DOYs 242–268, and ~2-days periodicities between DOYs 262–268.

The non-linear interactions are based on the theory of Teitelbaum and Vial (1991), who demonstrated that two oscillations with their respective pairs of primary zonal wavenumbers (s_1 and s_2) and frequencies ($n_1\Omega$ and $n_2\Omega$), where $\Omega = (2\pi/24)\mathrm{h}^{-1}$, can generate secondary waves with frequencies and zonal wavenumbers corresponding to the sum or difference of the primary waves. Specifically, the secondary waves have frequencies of $n_1\Omega + n_2\Omega$ or $n_1\Omega - n_2\Omega$ and zonal wavenumbers of $s_1 + s_2$ or $s_1 - s_2$. For example, a non-linear interaction between a migrating diurnal tide $(n = 1, s = 1)$ and a migrating semidiurnal tide $(n = 2, s = 2)$ can generate a migrating terdiurnal tide $(n = 3, s = 3)$, as described by Moudden and Forbes (2013). Similarly, the non-linear interaction between a tide and a PW1 can generate secondary waves with longer periods. PWs are long-period global oscillations that can generate secondary waves with periods of ~6 and ~10-days (Forbes and Zhang, 2015, 2017). In a study by Gu et al. (2016), the non-linear interaction between a westward-propagating wave with zonal wavenumber 3 (W3) and a stationary planetary wave with zonal wavenumber 1 (SP1) was simulated. The primary waves had frequencies (f) and wavenumbers (s) of (f, s) = (0.5, 3) and (0, 1), respectively. The authors found that this

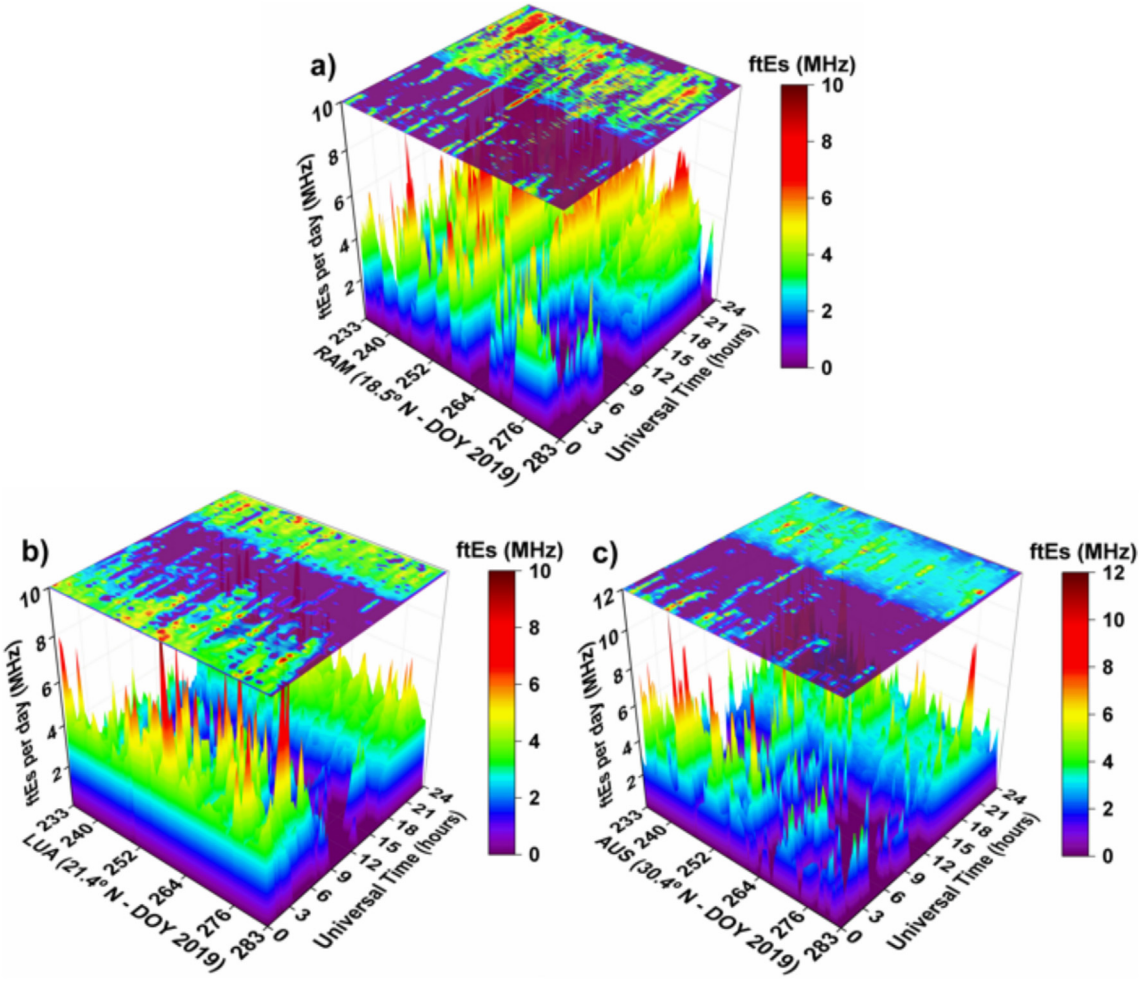

Fig. 6. The same as in Fig. 3, but for NH stations of (a) RAM, (b) LUA, and (c) AUS.

Table 3
Comparison between the highest *ftEs* values of the *Es* layers in the SH and NH of the American continent.

Comparison of the highest *ftEs* values			
Station (Code)	*ftEs* (MHz)	DOYs	Time (UT)
SJC	~12	281; 282	13:00; 03:00
JAT	~14 and ~17	263; 282	00:25; 14:30
ARA	~17 and ~20	248; 257	02:35; 23:00
RAM	~10	240; 257	18:00–22:00
LUA	~10	258; 279	01:00; 04:00
AUS	~12	244	00:15

interaction generated secondary waves with $(f, s) = (0.5, 4)$ and (0.5, 2), corresponding to oscillations with periods of approximately 4 and 2 days.

The evidence of the effects of the 2019 SSW on the *ftEs* parameter can also be seen in the 3D plots of Fig. 6 for the NH stations of RAM, LUA, and AUS. The daily and temporal variability of the *ftEs* observed at the station of RAM, located in the NH of the American continent, are shown in Fig. 6a. Frequency values above ~9 MHz from 17 to 23 UT is noted between DOYs 238–244, with maximum peaks of ~10 MHz being observed mostly between 18 and 22 UT on DOY 240 and 257.

The results for the stations of LUA and AUS, both located in the NH of the American continent, are shown in Fig. 6b and 6c, respectively. The maximum peak in *ftEs* for the station of LUA attained ~10 MHz (~01 UT) on DOY 258 and 279 (~04 UT), whereas for the station of AUS a maximum *ftEs* peak of ~12 MHz was observed at around 00:15 UT on DOY 244, the higher value of *ftEs* observed in the NH stations.

Table 3 summarizes the highest *ftEs* values of the *Es* layers observed at the stations located in the SH and NH of the American continent. It can be seen that the highest *ftEs* values during the 2019 SSW are in the SH at the JAT (~17 MHz) and ARA (~20 MHz) stations, but the NH stations also show atypical *ftEs* of ~10 MHz.

Analogous to what was done for the stations in South America, Fig. 7 shows the results of the wavelet power spectral analyses of the *ftEs* parameter, that reveal the characteristics of the PW oscillations observed over the NH stations of RAM, LUA, and AUS. Fig. 7a shows,

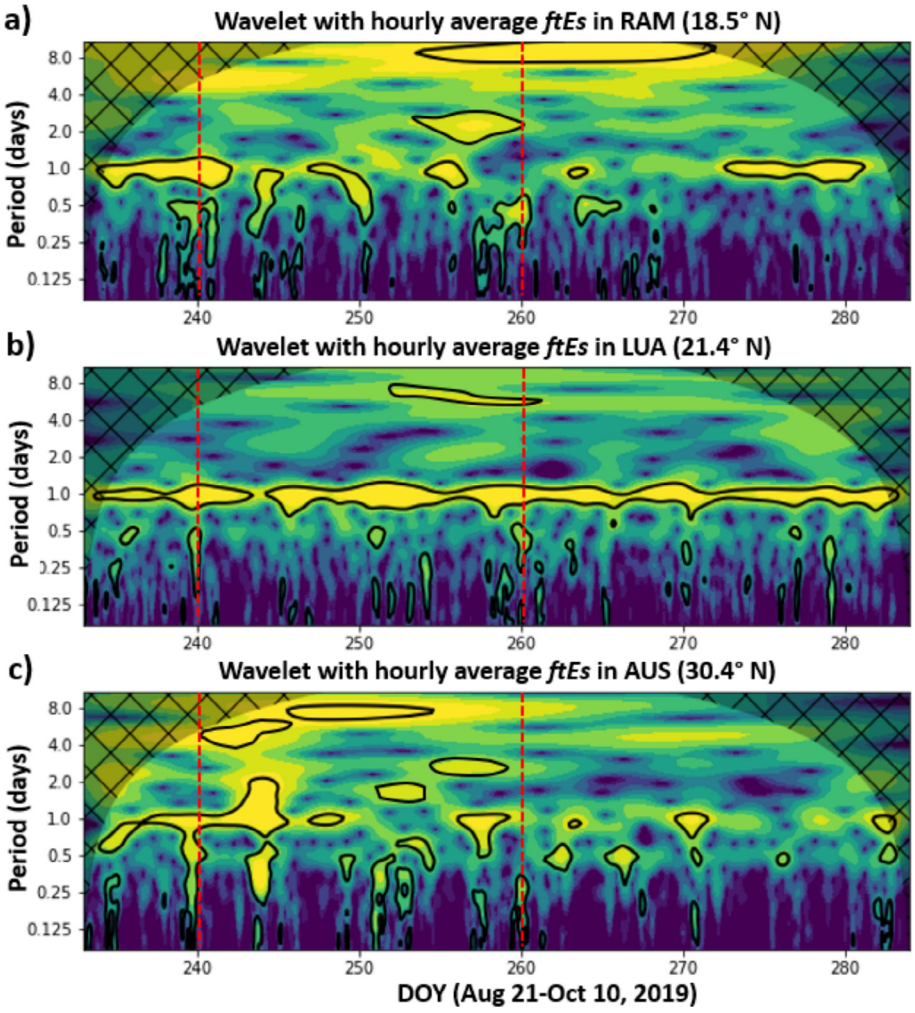

Fig. 7. Same as in Fig. 4, but for the NH stations of (a) RAM, (b) LUA, and (c) AUS.

Table 4
Comparison of PW oscillations over the *Es* layers in the SH and NH of the American continent.

Comparison of PW Oscillations across *Es* Layers		
Station (Code)	Period (days)	DOYs
SJC	~3–6	252–268
JAT	~2–6	258–268
ARA	~4–6; ~2	242–268; 262–268
RAM	~2; ~8	253–259; 253–272
LUA	~6–8	252–261
AUS	~8; ~4–6; ~2	245–255; 240–245; 242–245

for the RAM station, PW oscillations of ~2-days between DOYs 253–259. In addition to the ~2-days periodicities, there was a ~8-days oscillation between DOYs 253–272. Periodicities of ~6–8-days were observed over the station of LUA (Fig. 7b) between DOYs 252–261. The ~8-days oscillations can also be observed before the central day (DOY 240), between DOYs 245–255, at the observatory of AUS located furthest from the magnetic equator in the NH of the American continent, as shown in Fig. 7c. In addition to the ~8-days oscillations, PW waves with periodicities of ~4–6-days are observed in AUS between DOYs 240–245, and ~2-days between DOYs 242–245 and 251–259. Over these stations, it is possible that the dissipation of PWs was greater than in the SH as the waves propagated from high latitudes in the SH to low/mid latitudes in the NH (Goncharenko et al., 2021; Ma et al., 2022). It is also likely that at latitudes in the NH, the non-linear interactions between PWs and primary tidal winds were weaker, producing less intense secondary waves compared to the SH latitudes (Pancheva et al., 2009; Gu et al., 2018).

Table 4 summarizes the occurrence of PW oscillations over the *Es* layers of the stations located in the SH and NH of the American continent. It can be observed that during the SSW of 2019 on the American continent, the ~6-days PW oscillations are dominant over the *ftEs* at SH stations. On the other hand, at NH stations, the ~8-days oscillations dominate over the *ftEs*. The presence of these oscillations in the *ftEs* parameter across multiple stations in both hemispheres suggests a large-scale process influencing *Es* layer variability, likely driven by non-linear interactions between PWs and atmospheric tides. These interactions, as proposed by Teitelbaum and Vial (1991), can generate secondary waves with sum and difference frequencies of the primary waves, leading to enhanced electron densities in the *Es* layers. The widespread occurrence of these secondary waves supports their role in modifying *Es* layer behavior during the 2019 Antarctic SSW event, consistent with previous studies such as Haldoupis and Pancheva (2002) and Pancheva et al. (2003).

In the study of Goncharenko et al. (2021), the authors reported large regional anomalies corresponding to the behavior of the NH mid-latitude ionosphere during the 2019 Antarctic SSW event. They suggest that the ionospheric response is probably driven by $\sum O/N_2$ variations induced by tidal dissipation and PWs, variations in plasma drift due to the E region dynamo, and variations in the thermospheric wind. In addition, they emphasize the role of secondary waves generated by the interaction of the quasi-6-days wave and the tides. Ma et al. (2022) analyzed the global propagation of the Q6DW during the 2019 Antarctic SSW and observed that this wave is amplified by the SSW in an inter-hemispheric propagation. They found that interhemispheric propagation of Q6DWs contributed significantly to their enhanced development in both hemispheres. The analysis of the meridional circulation of metal ions in the lower thermosphere (100–120 km), at *Es* layer heights, was performed by Yu et al. (2021). The authors observed seasonal changes in density maxima consistent with inter-hemispheric transport. They showed an increase in Fe^+ ions between 105 and 115 km and ±45° latitude. They also observed that the maximum density occurs around 106 km in altitude, coinciding with the dominance of meridional circulation in the lower thermosphere. The peaks in *ftEs* values observed in Figs. 4 and 6 and Tables 2 and 3, can likely be attributed to the inter-hemispheric propagation of disturbances, which was amplified during the 2019 Antarctic SSW. Therefore, the enhanced development of these disturbances in both hemispheres may have contributed to the atypical values of *ftEs*. In addition, the accumulation of metallic ions, especially Fe^+, seems to have been disturbed, further influencing the anomalies observed in the heights of the *Es* layer.

3.3. Columns of O_3, H_2O, and the non-linear interaction between PW and tides during the 2019 Antarctic SSW

Atmospheric tides are driven primarily by the diurnal heating of the atmosphere due to solar radiation (infrared and ultraviolet) and the distribution of atmospheric mass. Molecular components like H_2O (water vapor) in the troposphere and O_3 (ozone) in the stratosphere play important roles in modulating the thermal structure and energy absorption, thereby influencing the overall dynamics of tidal winds (Hagan et al., 2009; Oberheide et al., 2011; Andrioli et al., 2022). The tides generated in the troposphere and stratosphere increase exponentially in amplitude and reach the lower thermosphere, where *Es* layers are formed via the horizontal neutral wind shear mechanism (Hagan and Forbes, 2002, 2003; Forbes and Wu, 2006; Forbes et al., 2008; Zhang et al., 2010a, 2010b; Forbes and Zhang, 2017; Lilienthal et al., 2018). Fig. 8 shows the observed values of the O_3 (black line), with concentration in the stratosphere (~30 km altitude), and H_2O (red line) columns, with concentration in the troposphere (~15 km altitude), and the zonal wind amplitude (U) (blue line, at ~30 km altitude) at mid- and low-latitudes in the SH during the 2019 Antarctic SSW event. The vertical yellow dashed line marks the onset of the 2019 SSW (DOY 240), while the vertical green dashed line indicates the lowest zonal wind speed (DOY 260) observed at 60°S and 10 hPa (~30 km altitude). The horizontal pink dashed line represents the zonal wind reversal point (U = 0).

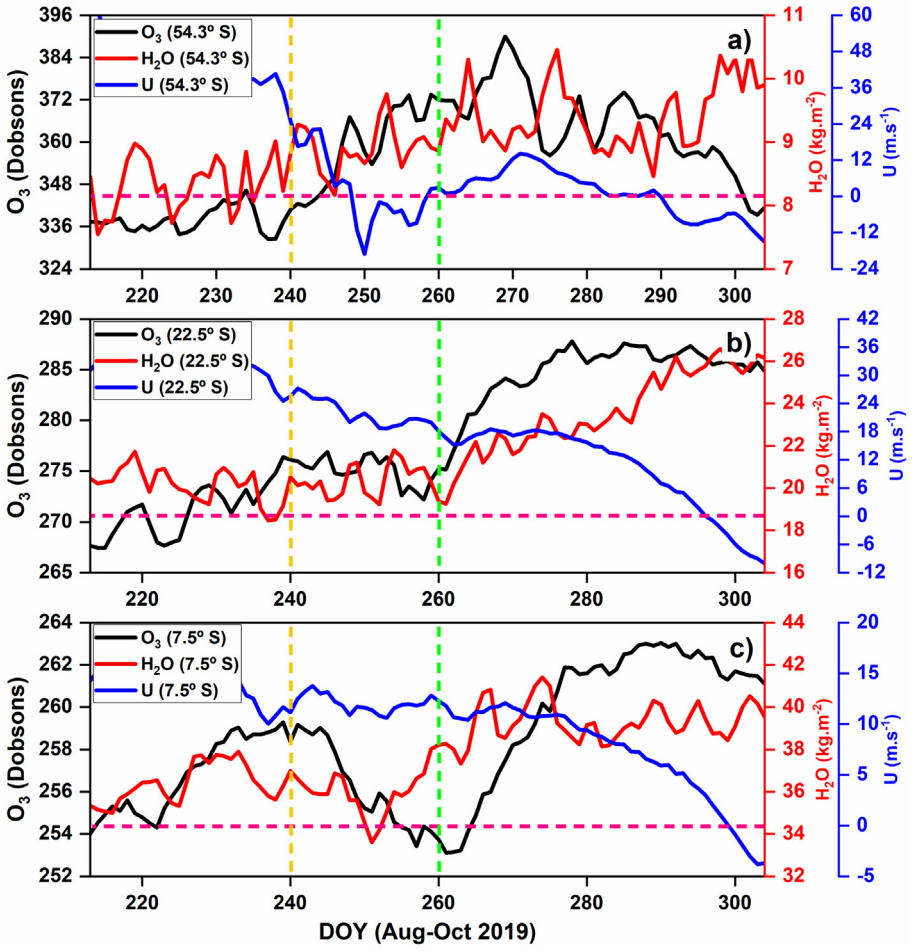

Fig. 8. Observation of ozone (black line) and water vapor (red line) columns, and zonal wind (blue line), during the 2019 Antarctic SSW event, in the mid- and low-latitude stations of the SH: (a) KEP, (b) CAP, and (c) JCA. The pink horizontal line corresponds to zero zonal wind speed. The vertical yellow line indicates the beginning of the SSW and the vertical green line indicates the central day of the event.

Fig. 8a shows that at the mid-latitude station of KEP, the zonal wind reversed (from west to east) on DOY 248, reaching a maximum eastward velocity of –19.1 m s^{-1} on DOY 250. Then the zonal wind reversed to westward on DOY 259 (~2.5 m s^{-1}), attaining ~14 m s^{-1} on DOY 271, and reversed again to eastward on DOY 290. This result for the zonal wind shown in Fig. 8a is in agreement with the study of Rao et al. (2020), who showed that a zonal wind inversion occurred at 50°S during the 2019 Antarctic SSW. Between DOYs 240–260 over KEP, as the zonal wind decreased in amplitude until it reversed and continued blowing eastward, a clear trend of increasing O_3 and H_2O columns was observed. The O_3 column increased from ~367 to 373 DU (Dobson Unit) and attained a maximum value of ~390 DU on DOY 269. Meanwhile, the H_2O column showed greater variation between the onset of the SSW event and the day of the lowest zonal wind speed, reaching a value of 9.7 kg m^{-2} on DOY 253. The H_2O column reached a value of 10.3 kg m^{-2} on DOY 264. The maximum value of ~10.5 kg m^{-2} in the H_2O column occurred on DOY 276.

Over the low latitude stations of CAP (Fig. 8b) and JCA (Fig. 8c), the results show that zonal wind did not reverse eastward between DOYs 240–260. Meanwhile, significant increases in the O_3 and H_2O columns are observed after the central day (DOY 260) of the SSW event. The increase in the total O_3 column observed in Fig. 8a (KEP station) before and after the central day, as well as after the central day for the stations of CAP (Fig. 8b) and JCA (Fig. 8c), is consistent with the increases of 29 % in September and 28 % in October reported by Safieddine et al. (2020). According to Shams et al. (2022) during SSW events the total O_3 column in the stratosphere may increase between around 9–29 %. Such an increase may last for about two months. According to Veenus et al. (2023), O_3 levels increase in the tropical upper stratosphere during an SSW event, driven by the phenomenon of vortex deceleration. On the other hand, Shen et al. (2020) observed that the Antarctic SSW of 2019 slowed down catalytic chemical reactions in the stratosphere that prevent ozone destruction, while increasing the molecular vibrations of these constituents, which contribute to tidal generation. In addition

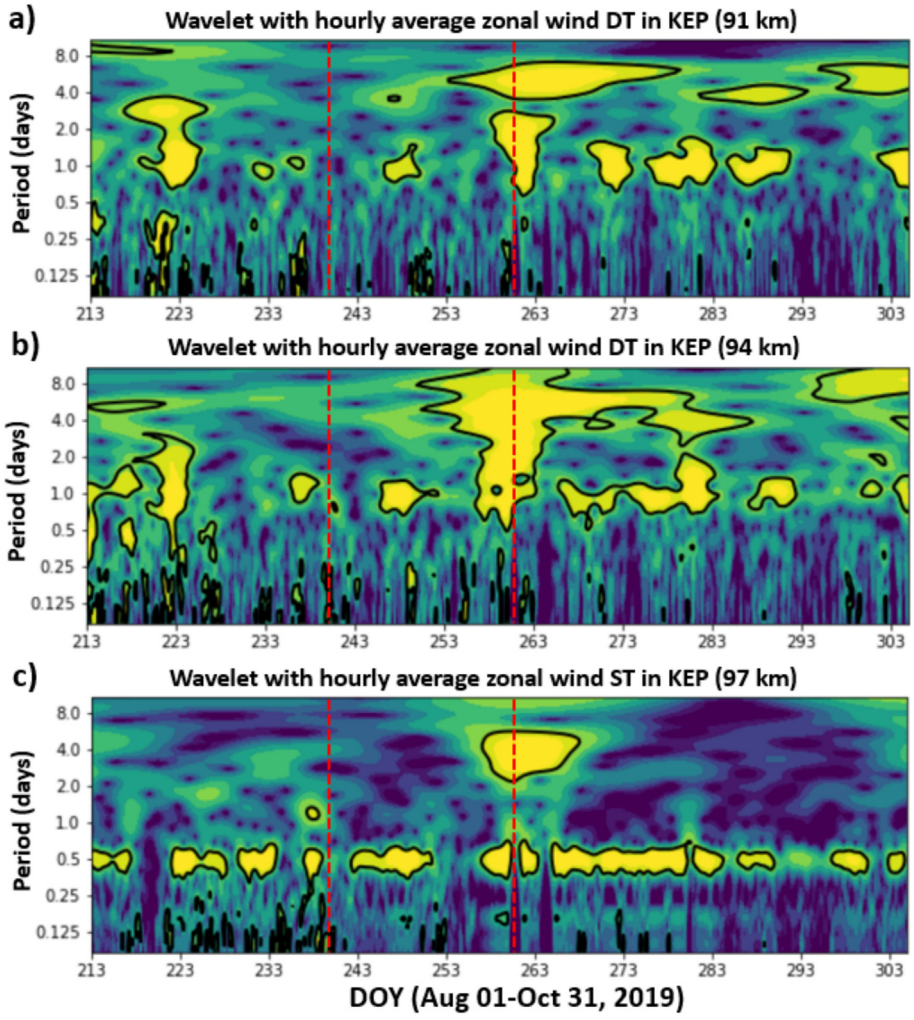

Fig. 9. Wavelet power spectrum analysis of the hourly mean values of zonal wind during the 2019 Antarctic SSW event (between DOYs 213–304, 2019) obtained at KEP for the: (a) zonal wind with the DT component at an altitude of 91 km, (b) zonal wind with the DT component at an altitude of 94 km, and (c) zonal wind with the ST component at an altitude of 97 km. The first vertical dashed line in red marks the onset of the 2019 Antarctic SSW event, and the second line corresponds to the central day of the event (DOY 240). The wavelet power spectral has been normalized to a 95 % confidence level, with the black contour lines representing the significant spectral peaks.

to the increase in the total O_3 column, the increase in the H_2O column at the latitudes of the stations shown in Fig. 8 is also consistent with Veenus and Das (2024), who showed an increase in the water vapor mixing ratio of ~25 % in the polar lower stratosphere and ~10 % in the tropical upper stratosphere. It is known that the increase in O_3 and H_2O columns during SSWs can lead to an increase in tides (Goncharenko et al., 2012; Limpasuvan et al., 2016; Siddiqui et al., 2019; Veenus and Das, 2024). Mitra et al. (2023) analyzed the behavior of equatorial-, low-, mid-, and high-latitude tides over the SH in the American continent during the 2019 Antarctic SSW. The authors found variability in diurnal and semidiurnal tidal amplitudes, consistent with global modes of DW1, DE3, and SW2 components, which may be related to the vertical distribution of O_3 and H_2O, as well as the zonal wind.

Fig. 9 shows the wavelet power spectrum analyses for the hourly zonal wind averages of the diurnal (DT) and semidiurnal (ST) tidal components obtained between DOYs 213–304, using data from the SkiYMET radar located at the observatory of KEP. Fig. 9a and b show that the diurnal component of the zonal wind (U) is present at 91 and 94 km above KEP. Fig. 9c shows the presence of the ST component of the zonal wind over KEP at an altitude of 97 km. In addition to these tidal components, the characteristic PW oscillations can be observed in Fig. 9a, with periods of ~4–8-days between DOYs 253–278, and after DOY 293. In addition, periodicities of ~4-days are observed between DOYs 283–293. Fig. 9b shows periodic oscillations of ~2–8-days between DOYs 250–267 and ~4–6-days until DOY 285. The ST component also showed PW oscillations between DOYs 257 and 268 with periods of ~2–6-days, as shown in Fig. 9c. The wavelet analyses

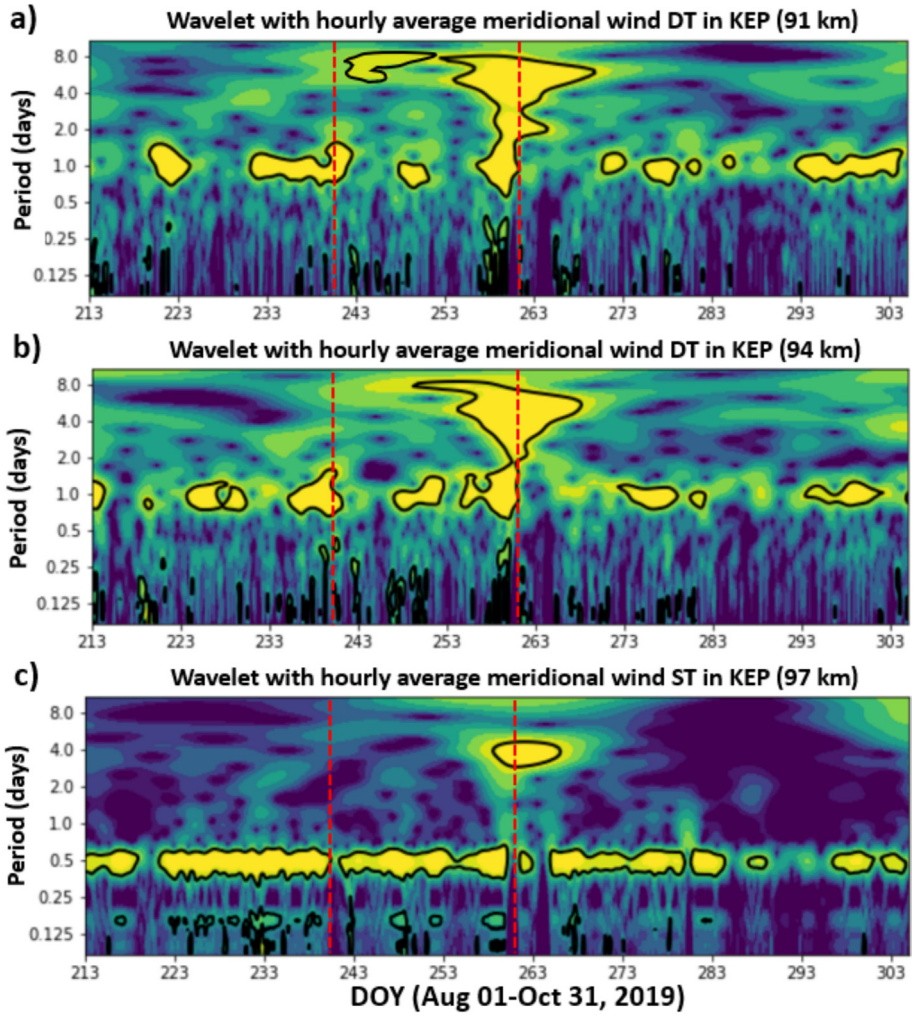

Fig. 10. Same as in Fig. 9, but for the meridional wind.

reveal oscillations with periods of 2–8-days, which are attributed to the non-linear interaction between PW1 and atmospheric tides. These secondary waves modulate the wind shear in the lower thermosphere, leading to the observed variability in the *Es* layers.

In addition to the zonal wind, the meridional wind (V) over the KEP observatory also showed PW oscillations with both the primary DT and ST components during the time interval of interest in this study (DOYs 240–283). Fig. 10a and 10b show that the ~2–8-days PW oscillations are present between DOYs 242–272, with the hourly mean of the daytime component of the meridional wind at 91 and 94 km height. The ST component (Fig. 10c) also showed a PW oscillation with the meridional wind with a period of ~4-days, but over a shorter time interval (between DOYs 258–267) than the DT component.

Fig. 11 shows the wavelet power spectrum analyses for the DT and ST tidal components of the zonal wind obtained for the low latitude stations of CAP and JCA. In the station of CAP, Fig. 11a shows the PW oscillations in the DT component with periods of ~4–6-days between DOYs 244–273 at an altitude of 93 km. In the station of JCA, Fig. 11b and 11c show PW oscillations with periods of ~4–6-days in the DT component of the zonal wind at 90 and 96 km, respectively, between DOYs 242–274. Fig. 11d shows PW oscillations with a period of ~4–6-days for the ST component of the zonal wind at 93 km altitude between DOYs 255–270.

The wavelet analyses shown in Figs. 9–11 are consistent with the observations of Mitra et al. (2023), as they showed the periodicity of the DT and ST with the zonal and meridional winds over mid- and low-latitudes and near the magnetic equator. Furthermore, characteristic PW oscillations can be observed, which are consistent with the oscillations over *ftEs*, demonstrating that the Antarctic SSW event of 2019 contributed to the dynamics of stratosphere-lower atmosphere coupling. The effects of the 2019 Antarctic SSW on PW with oscillations of ~4-days and ~6-days have also been reported in other recent studies (Miyoshi and Yamazaki, 2020; Yamazaki et al., 2020; Goncharenko et al., 2020; Eswaraiah et al., 2020; Ma et al., 2022; Luo et al., 2023). The results of the wavelet analyses of the *ftEs* and the tidal winds shown here are consistent with the work of Eswaraiah et al. (2020), who observed PW

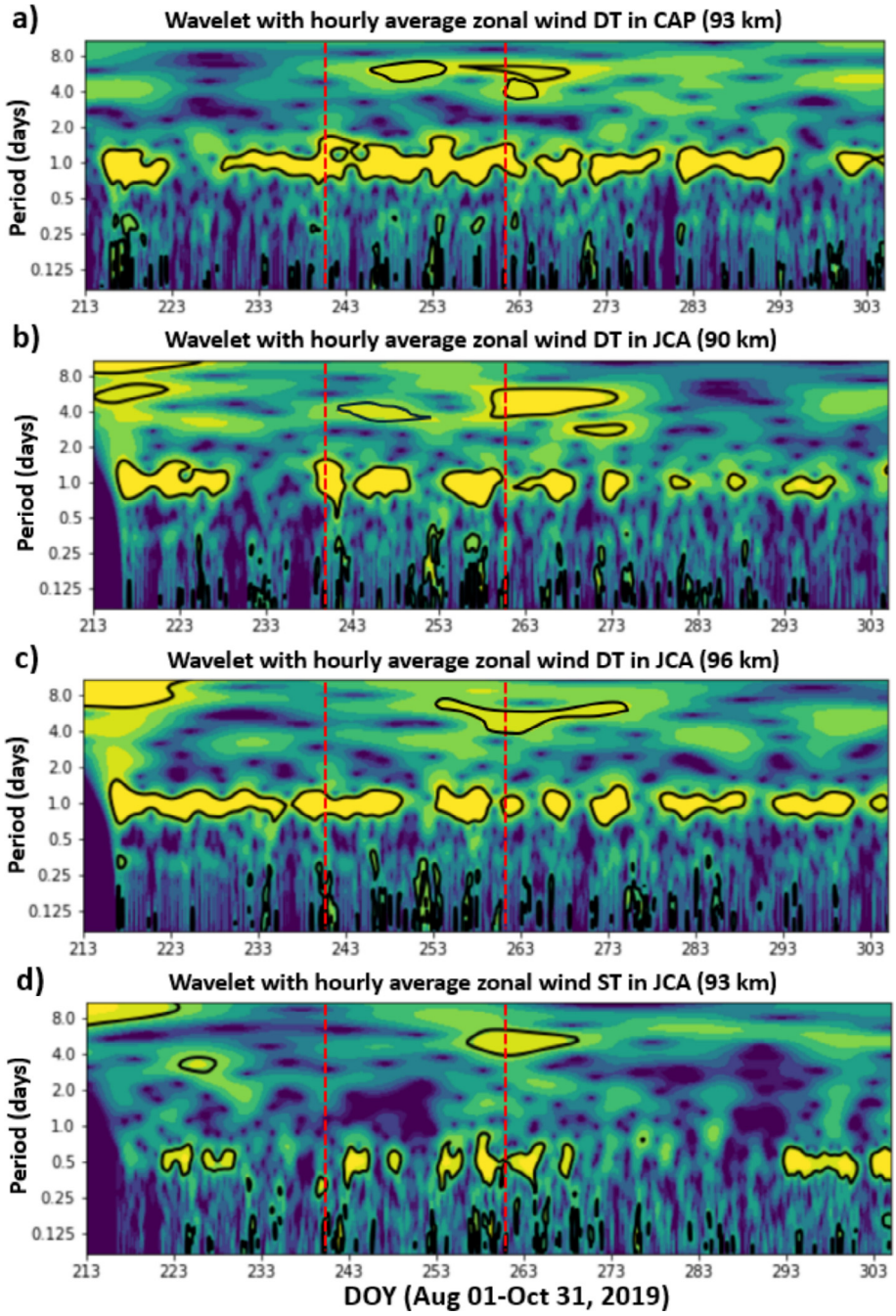

Fig. 11. Same as in Fig. 8, but for CAP and JCA, with: (a) zonal wind with the DT component at 93 km height over CAP, (b) zonal wind with the DT component at 90 km height over JCA, (c) zonal wind with the DT component at 96 km height over JCA, and (d) zonal wind with the ST component at 93 km height over JCA.

oscillations with waves of ~4–6-days in the zonal winds during the 2019 Antarctic SSW. Luo et al. (2023) observed strong activity of the ~4-days eastward propagating wave (E4DW) in early September 2019 in the SH, with an amplitude reaching ~20 m/s on September 7. Goncharenko et al. (2020) who analyzed ionospheric anomalies during the 2019 Antarctic SSW using total electron content (TEC), found strong oscillations of ~2–3-days and ~5–6-days between ±40° latitude range on the American, African, and Asian continents. The results of the wavelet analyses in Figs. 9, 10, and 11 for the zonal wind with the DT are consistent with the ~6-days PW oscillations shown in Miyoshi and Yamazaki (2020), who found this periodicity between September 13 and October 3 with a maximum amplitude at 95 km altitude between ±45° latitude.

It is worth recalling that although PWs oscillations over the *ftEs* are present within the estimated period of the 2019 Antarctic SSW (DOYs 240–283, Fig. 2), as shown in Figs. 5 and 7, and summarized in Tables 3 and 4, PW1 showed high amplitude values (1000–1500 m) between DOYs

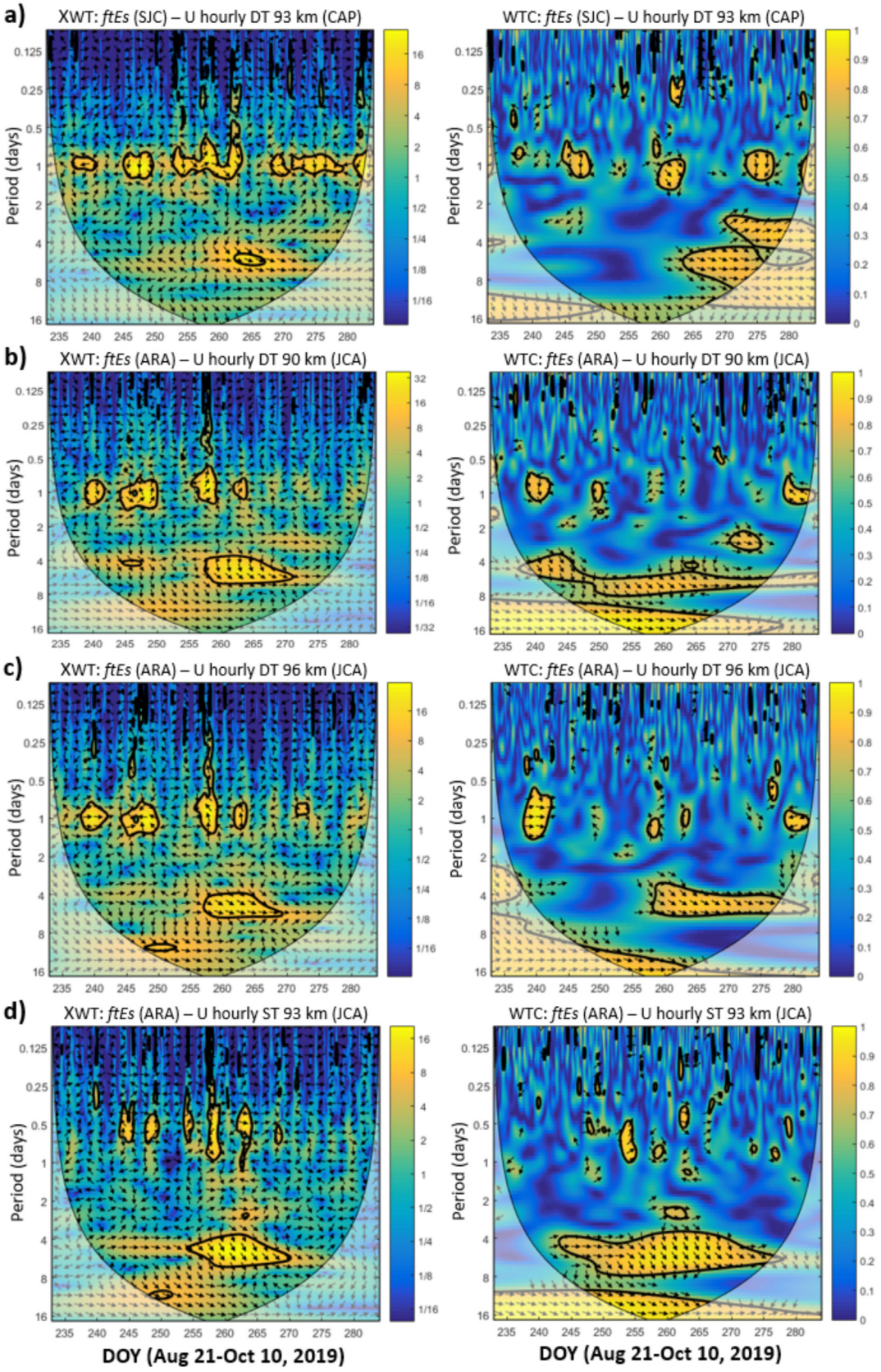
a)
XWT: ftEs (SJC) – U hourly DT 93 km (CAP)
WTC: ftEs (SJC) – U hourly DT 93 km (CAP)
b)
XWT: ftEs (ARA) – U hourly DT 90 km (JCA)
WTC: ftEs (ARA) – U hourly DT 90 km (JCA)
c)
XWT: ftEs (ARA) – U hourly DT 96 km (JCA)
WTC: ftEs (ARA) – U hourly DT 96 km (JCA)
d)
XWT: ftEs (ARA) – U hourly ST 93 km (JCA)
WTC: ftEs (ARA) – U hourly ST 93 km (JCA)
Period (days)
DOY (Aug 21-Oct 10, 2019)

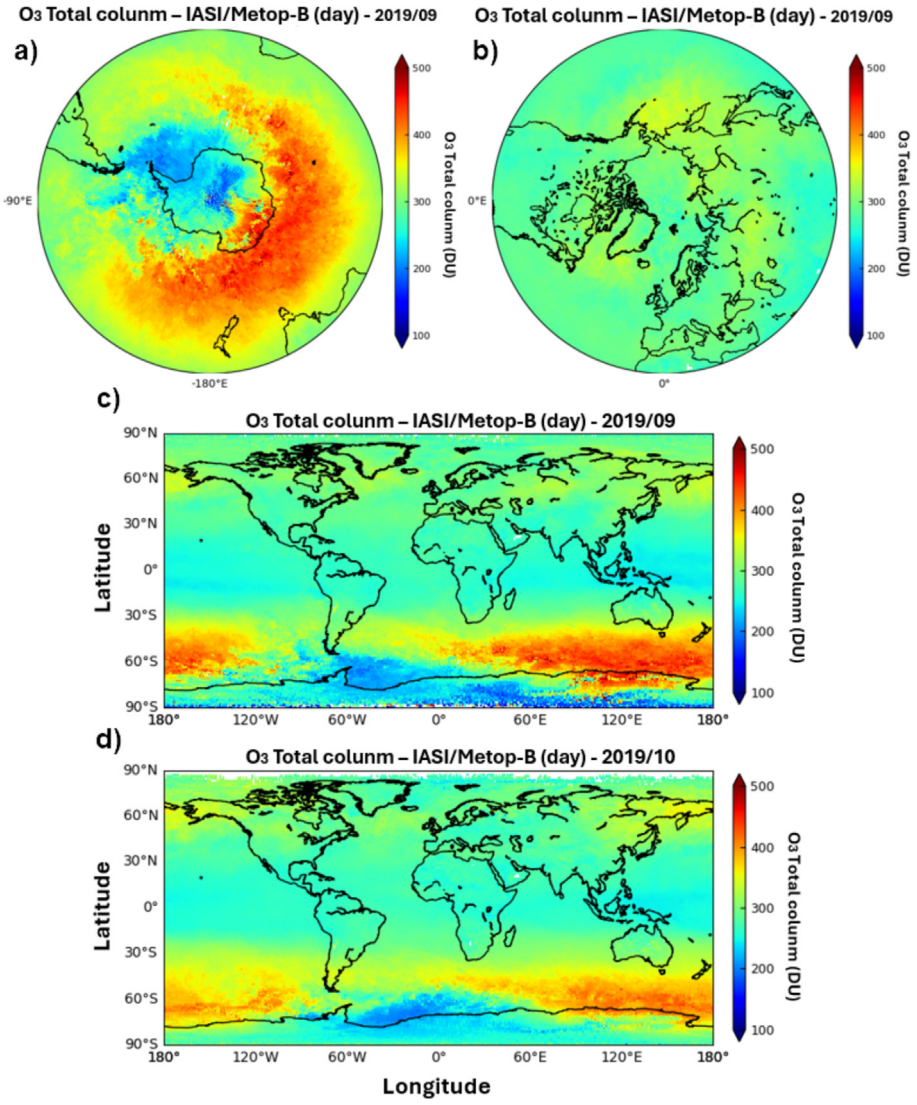

Fig. 13. (a) O_3 total column at the South Pole in September 2019; (b) O_3 total column at the North Pole in September 2019; (c) Global distribution of the O_3 total column in September 2019; and (d) Global distribution of the O_3 total column in October 2019.

221–232, well before the onset of the event. This could imply a non-linear interaction between PW1 and the tidal winds prior to the onset of the 2019 SSW, as seen in the diurnal zonal winds in Fig. 9a-9b and 10b-10c. However, wavelet analyses of the diurnal zonal winds show that these PW oscillations decrease with height. This strongly indicates that the PWs oscillations observed prior to the onset of the 2019 SSW did not have sufficient strength to reach the lower thermosphere, as their amplitude and energy were dissipated by the plasma before reaching the E region. However, it was only when the 2019 Antarctic SSW began, and PW1 reached very high amplitude values (1500–2180 m), that the oscillations of the PWs resulting from the non-linear interaction between PW1 and the tides,

Fig. 12. Like the sequence in Fig. 11, where the Cross-Wavelet Transform (XWT, left) and the Wavelet Transform Coherence (WTC, right) were used to show the correlation between the ftEs and the tidal wind series, with: (a) ftEs over SJC and DT zonal wind over CAP (93 km high), (b) ftEs over ARA and DT zonal wind over JCA (90 km high), (c) ftEs over ARA and DT zonal wind over JCA (at 96 km high), and (d) ftEs over ARA and ST zonal wind over JCA (93 km high). The thick black contours indicate the 95 % confidence level, and the transparent region indicates the cone of influence (COI). The XWT color bar indicates the power of the cross-spectrum (intersection between ftEs and winds), and the WTC color bar corresponds to the confidence level of the Monte Carlo test. The arrows indicate the phase relationship of the two series in time–frequency space ($\geq 60\%$), where: (i) the arrows pointing to the right indicate in-phase behavior; (ii) The arrows pointing to the left indicate anti-phase behavior; (iii) The downward pointing arrows indicate that the ftEs peak series lags behind the wind series by 90°; (iv) The arrows pointing up indicate that the ftEs peak series leads the wind series by 90°.

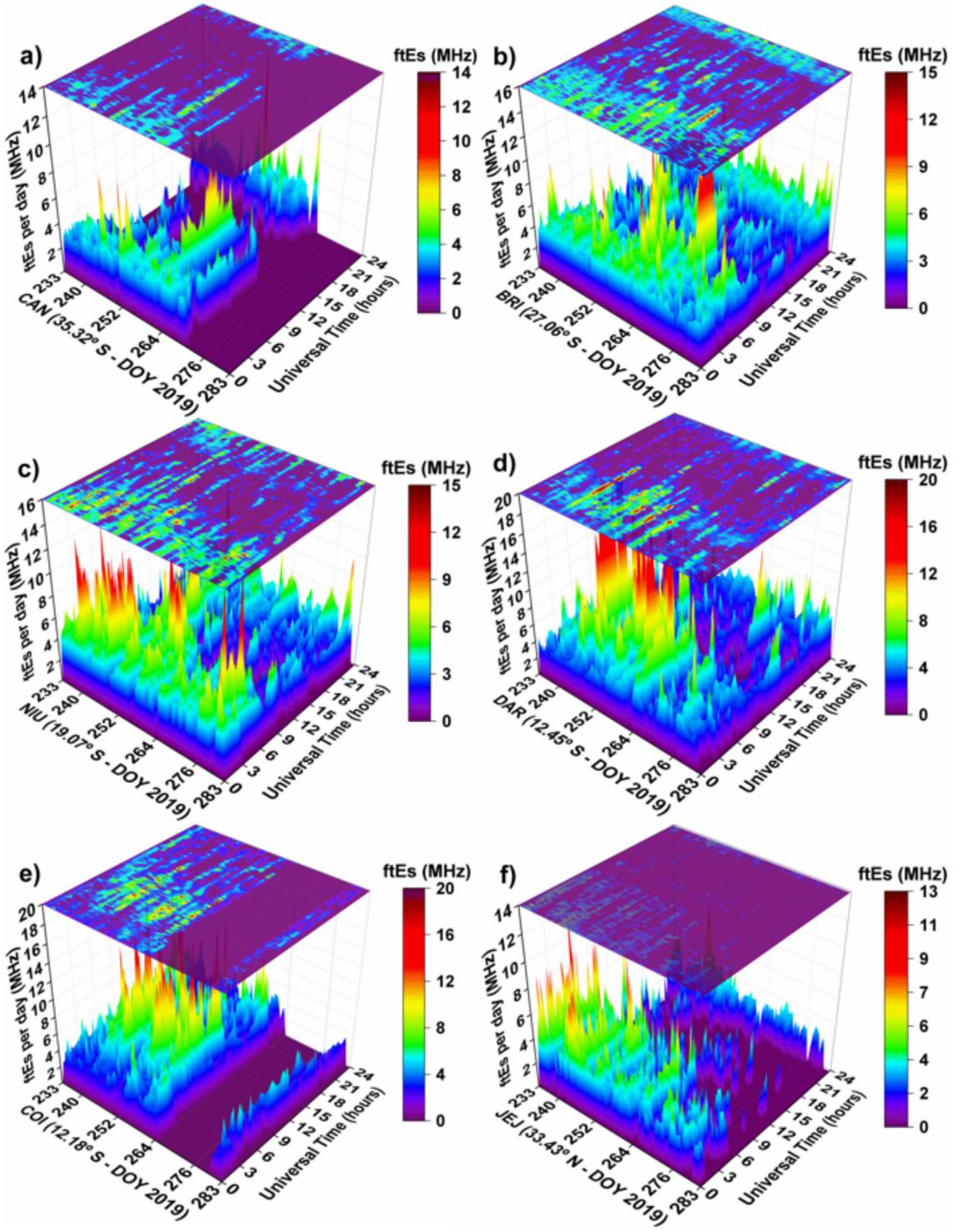

Fig. 14. 3D plots of the daily and temporal variability of the ftEs parameter observed during the 2019 Antarctic SSW event in the stations of (a) CAN, (b) BRI, (c) NIU, (d) DAR, (e) COI, and (f) JEJ, located in the Oceanian (Australian) or Asian sectors. The ftEs values were colored according to the scale shown on the bars, with the highest value in the range being the maximum peak in ftEs observed at that station.

propagated into the lower thermosphere and contributed to the formation of the *Es* layers. This interaction led to significant peaks in *ftEs*, as shown in Figs. 4 and 6. Furthermore, tidal winds are global phenomena and exhibit minimal variation between nearby stations, indicating that the tidal wind observed in JCA can be utilized to assess its effects on *ftEs* parameters over ARA. This phenomenon is also evident at the CAP and SJC observatories.

Consequently, it is reasonable to use *ftEs* and tidal wind data from nearby locations to demonstrate a correlation between these parameters.

Cross-wavelet transform (XWT) and wavelet transform coherence (WTC) analyses can be used to find the correlation and phase coherence between two wavelet series, e.g., *ftEs* (Fig. 5) and wind (Fig. 11), in the time–frequency domain. These methods can also be used to highlight common significant periodicities, even when the cross-wavelet power is as low as ~5 % (Grinsted et al., 2004). Fig. 12 shows the XWT and WTC analyses between the wavelet series of the *ftEs* and the tidal wind components. Fig. 12a shows correlation (XWT) and phase coherence (WTC) with common periodicities between the *ftEs* wavelet series over SJC and the zonal component of the DT wind over CAP (93 km high), with stronger evidence between DOYs 260–267. A periodicity of ~4–6-days is observed when the two series are in-phase, which is consistent with the results shown in Figs. 5a and 11a. Similarly, a periodicity of ~4–8-days (with phase ≥60 %) is observed in the XWT and WTC analyses between the *ftEs* series over the ARA and the DT zonal wind over the JCA (Fig. 12b and c), with greater intensity between DOYs 256–272. Additionally, a coherence and correlation in the ~3–6-days periodicity range can be observed between the *ftEs* series and the ST zonal wind at the latitudes of ARA and JCA (Fig. 12b–d) between DOYs 254–270. These XWT and WTC results (Fig. 12b–d) are well aligned with the wavelet series seen in Figs. 5c and 11b–d, demonstrating a strong correlation and phase coherence between the two *ftEs* wavelet series and the DT and ST wind components.

3.4. Global O_3 column, atypical ftEs peaks, and PW oscillations in the Es layers over the Oceanian (Australian) and the Asian sectors

Shen et al. (2020) showed that the westward slowing of the polar jet in the Antarctic SSW of 2019 increased the mixing of high O_3-density air at mid-latitudes. In addition, the authors observed that the Antarctic ozone hole was smaller during this SSW compared to the two major SSW events of 1988 and 2002 in the SH. Roy et al. (2022) reported that the polar vortex was displaced during the Antarctic SSW of 2019, which may have contributed to the global spread of O_3 towards the mid-latitudes. The panels a–d in Fig. 13 show that the increase in the total O_3 column observed during the 2019 Antarctic SSW event was not limited to the polar region but extended globally.

It was observed that the total O_3 column over the Australian sector, close to the South Pole (Fig. 13a), was stronger during September with ~400–500 DU compared to the North Pole (Fig. 13b), which showed ~300–320 DU. Furthermore, at mid and high latitudes during the month of September (Fig. 13c), this column is also much stronger over the Australian region than over South America. In October (Fig. 13d) also showed a stronger total O_3 column over the Australian region than over the American continent, but this difference was smaller compared to September. Comparable increases in water vapor likely occurred over the Australian region (not shown here), as well as over the South American continent, as depicted in Fig. 8. The results for the global distribution of O_3 are consistent with the ±60° increase in ozone shown in Veenus and Das (2024). The authors also showed that there was an increase in water vapor (H_2O) between ±60°.

Fig. 14 shows the *ftEs* values (in MHz) observed at the stations located in the Oceanian (Australian sector) and Asian continents. The zero *ftEs* values in Fig. 14a between DOYs 271–283 and Fig. 14e between DOYs 265–280 were due to equipment problems. Fig. 14a shows the results of the *ftEs* for the CAN station during the 2019 Antarctic SSW, where it can be observed that the *ftEs* reached a maximum peak of ~14 MHz around ~21 UT on DOY 257. On the other days, *ftEs* in CAN reached values of the order of ~9 MHz. At the BRI station (Fig. 14b), *ftEs* reached a maximum value of ~15 MHz between 06 and 09 UT on DOY 271, when the frequencies were already fluctuating around 10 MHz. Other peak values in *ftEs* above ~10 MHz were also observed at BRI between DOYs 251–263.

For the station of NIU (Fig. 14c), it is noted that at the end of the 2019 Antarctic SSW, around 05 UT on DOY 279, a peak value of ~15 MHz in *ftEs* occurred. Frequencies of ~14 MHz were observed at ~03 UT on DOY 277, with values above 11 MHz also recorded at the beginning of the event, as well as before and after the central day (DOY 260), specifically between DOYs 240–244, and from DOYs 252–261. On the other hand, in the station of DAR (Fig. 14d), it is possible to observe maximum peaks

Table 5
Comparison between the highest *ftEs* values of the *Es* layers in the SH and NH of the Oceania and Asian continents.

Comparison of the highest *ftEs* values			
Station (Code)	*ftEs* (MHz)	DOYs	Time (UT)
CAN	~14	257	21:00
BRI	~15	271	06:00–09:00
NIU	~15; ~14	279; 277	05:00; 03:00
DAR	~20	245; 257	05:00–09:00; 04:00–07:00
COI	~20; ~16; ~17	245; 255; 261	09:30; 17:00; 09:00
JEJ	~13	234	06:00

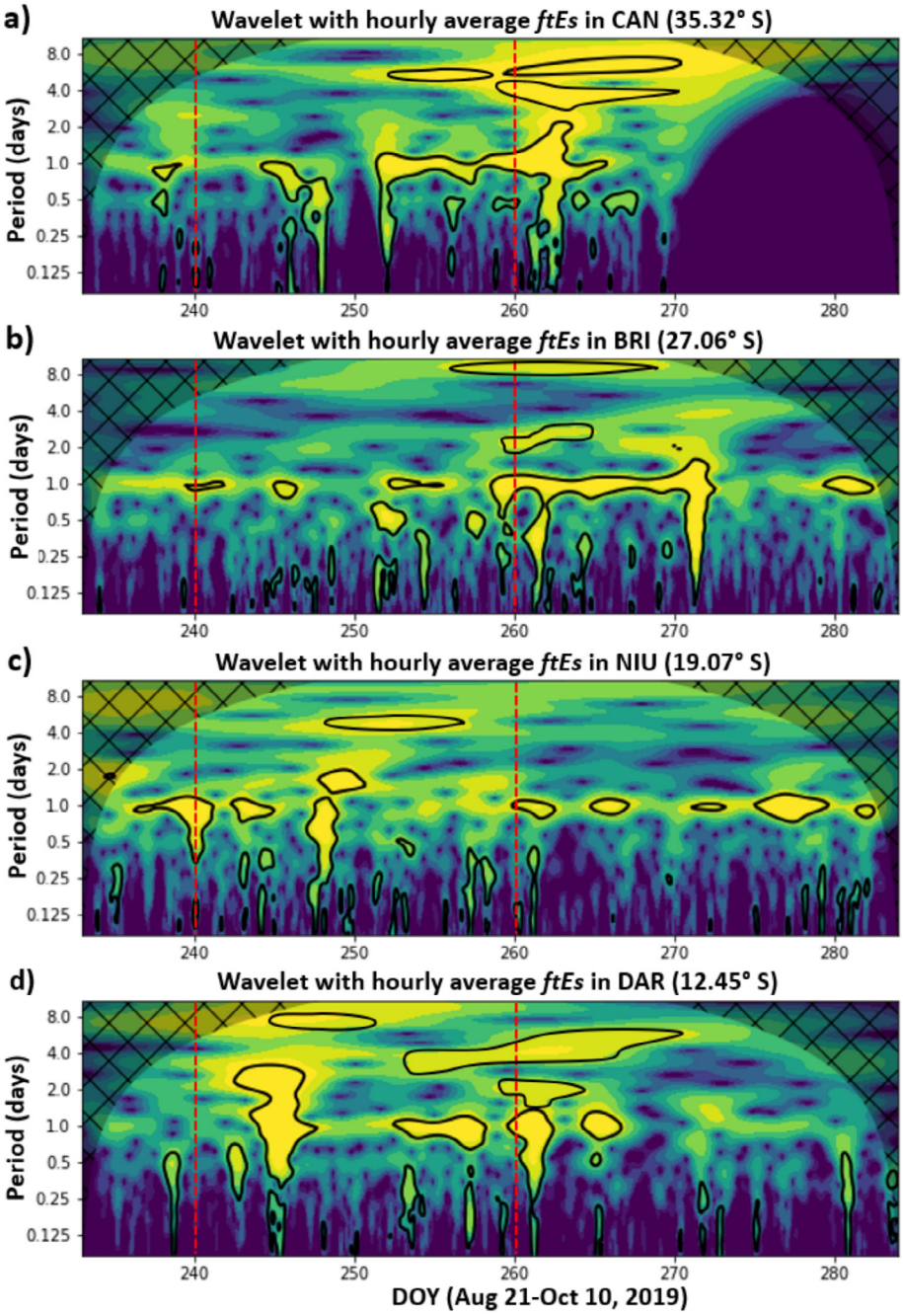

Fig. 15. Wavelet power spectrum analysis of the ftEs parameter during the 2019 Antarctic SSW event at: (a) CAN, (b) BRI, (c) NIU, and (d) DAR. The first vertical dashed line in red corresponds to the start of the event (DOY 240), and the second line corresponds to the central day of the event (DOY 260). The wavelet power spectral has been normalized to a 95% confidence level, with the black contour lines representing the significant spectral peaks.

Table 6
Comparison of PW oscillations over the *Es* layers in the SH and NH of the Oceanian and Asian continents.

Comparison of PW Oscillations across *Es* Layers		
Station (Code)	Period (days)	DOYs
CAN	~3–8; ~2	252–271; 262
BRI	~8; ~2	256–270; 259–265
NIU	~2; ~4–6	247–257
DAR	~2; ~4–6; ~8	241–249; 258–265; 253–271; 245–252
COI	~4–8; ~2	242–252; 261
JEJ	~8; ~4–6; ~2	245–255; 240–245; 242–245

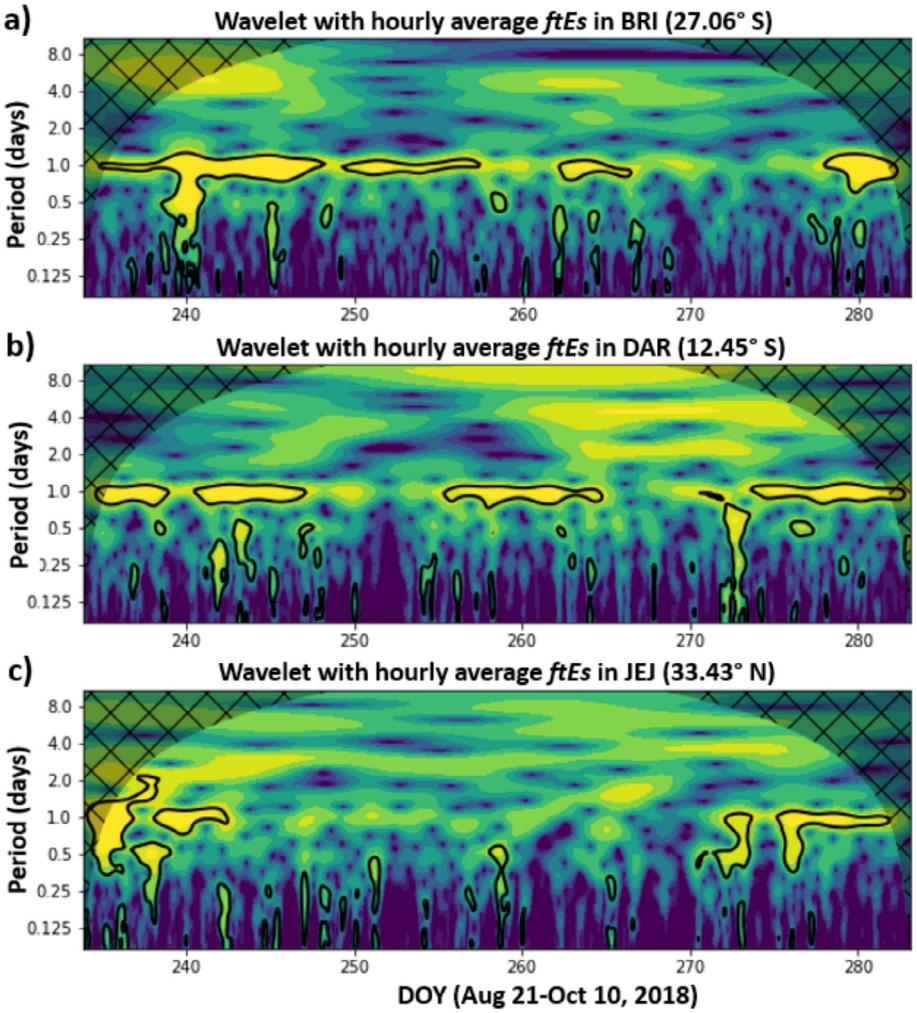

Fig. 16. Wavelet power spectrum analysis of the ftEs parameter for the period from August 21 to October 10, 2018, when no SSW event occurred, demonstrating the absence of the 2–8-days periodicities at: (a) BRI, (b) DAR, and (c) JEJ. The wavelet power spectral has been normalized to a 95% confidence level, with the black contour lines representing the significant spectral peaks.

of *ftEs* at ~20 MHz occurring between 05 and 09 UT on DOY 245, and also before the central day between around 04–07 UT on DOY 257.

Atypical *ftEs* values were also observed for the COI station (Fig. 14e) located in the SH of the Oceanian continent. At the COI station, the maximum *ftEs* peak of ~20 MHz was observed at 09:30 UT on DOY 245, a peak of ~15 MHz at 10 UT (DOY 254) and ~16 MHz at 17 UT (DOY 255) before the central day (DOY 260), and a peak of ~17 MHz between 08 and 09 UT on DOY 261. The JEJ station showed a maximum of ~13 MHz (06 UT) on DOY 234, probably due to a PW of ~2–4-days that occurred between DOYs 232–240. It was not possible to determine why this PW oscillation, probably due to non-linear interaction with the tides, occurred well before the onset of SSW. However, there was another peak of *ftEs*, slightly lower than the first one with ~11 MHz (06:30 UT) before the central day (DOY 251), and another of ~10 MHz (05:45 UT) after the central day.

Table 5 summarizes the highest *ftEs* values of the *Es* layers for the stations located in the SH and NH of the Oceanian and Asian continents. It can be observed that the highest *ftEs* values during the 2019 SSW on the Oceanian continent are at the stations closest to the magnetic equator, DAR (~20 MHz) and COI (~20 MHz), while the other stations on this continent show atypical *ftEs* of ~14 MHz.

Analogous to what was done for the stations located on the American continent, panels (a–d) of Fig. 15 show the characteristics of the PW oscillations obtained from the wavelet power spectrum analysis of the *ftEs* parameter collected at the stations located in the SH of the Oceanian continent (Australian sector). At the station of CAN (Fig. 15a), periodicities between ~3–8-days are observed from DOYs 252 to 271, and ~2-days around DOY 262. The ~8-days oscillation remains at the station of BRI (Fig. 15b) between DOYs 256–270, and periodicities of ~2-days between DOYs 259–265. In the stations of CAN and BRI, the PW oscillations are observed before and after

the central day (DOY 260) of the 2019 Antarctic SSW event. At the station of NIU (Fig. 15c), periodicities of ~2-days and ~4–6-days are observed before the central day between about DOYs 247 and 257. On the other hand, at the DAR station (Fig. 15d), PW oscillations are seen before and after DOY 260. For example, ~2-days oscillations are noticed between DOYs 241–249 and 258–265. However, the most prominent oscillations are around 4–6-days and occurred between DOYs 253–271. Additionally, ~8-days periodicities were observed between DOYs 245–252.

Table 6 summarizes the occurrence of PW oscillations over the *Es* layers of the stations located in the SH and NH of the Oceanian and Asian continents. It can be observed that during the 2019 SSW on the Oceanian continent, the ~8-days PW oscillations are dominant over the *ftEs* at the CAN and BRI stations. While at the stations of NIU, DAR, and COI, PW oscillations of ~4–6-days predominate in the SH. On the other hand, in the JEJ (NH) station, the ~8-days oscillations dominate for longer in the *ftEs*.

It is also worth mentioning that the diurnal periodicity is observed at all stations in Fig. 15, and on certain days, semidiurnal or even lower periodicities are also noticeable. Therefore, the results suggest that a strong interaction between the primary tides and PWs may have resulted in the pronounced peaks observed in the *ftEs* values at some stations (Figs 4, 6 and 14), ranging between ~14 and 20 MHz. The interaction between the tides and PWs has been observed in several studies, such as the work by Mitra et al. (2023), who highlighted the influence of the diurnal and semidiurnal tides on zonal and meridional winds over mid- and low-latitudes. Over the Australian sector, the *ftEs* peaks observed were significantly higher (Fig. 14), probably due to stronger interactions between the tides and PWs in this region, compared to the other areas analyzed here. An exception was observed at the ARA station in the SH of the American continent, which exhibited an *ftEs* peak around ~20 MHz, potentially related to enhanced local dynamics (see Fig. 3). The results shown in Figs. 14 and 15 are consistent with the wavelet analyses presented in Figs. 9-11, which suggest a broader coupling between the stratosphere and lower atmosphere during the 2019 Antarctic SSW event, influencing the propagation of PWs and their interaction with the *Es* layer. Finally, the analyses of peak *ftEs* and wavelets of *ftEs* over the Oceanian/Asian continents indicate that the non-linear interaction between tides and PWs occurred on a global scale, generating secondary oscillations ranging from ~2 to 8-days. This finding is in accordance with the recent studies of Miyoshi and Yamazaki (2020), Yamazaki et al. (2020), Goncharenko et al. (2020), Eswaraiah et al. (2020), Ma et al. (2022), and Luo et al. (2023).

The wavelet power spectral analyses shown here reveal the temporal differences and amplitude variations of the *Es* layer oscillations at different stations, even within the same sector. This can be attributed to several factors. First, the nonlinear interaction between PWs and atmospheric tides can vary spatially due to differences in the local atmospheric dynamics, such as zonal and meridional winds, which modulate the propagation and amplitude of PWs (Palo et al., 2005). Furthermore, the variability in *Es* layer electron density is influenced by the distribution of metallic ions, which can be affected by interhemispheric transport processes and meridional circulation in the lower thermosphere (Yu et al., 2021). Previous studies, such as Mo and Zhang (2020), have demonstrated that the modulation of PWs in the ionosphere can exhibit significant temporal differences between regions, even during SSW events, due to the complex interaction between PWs and tides. Yamazaki et al. (2020) also highlighted that PW dissipation and its interaction with tides can vary with latitude and altitude, resulting in distinct oscillation patterns. Therefore, the differences observed and summarized in Tables 4 and 6 reflect the complex and global nature of the interaction between PWs and the ionosphere during SSW events. It is also important to highlight that weak geomagnetic disturbances occurred during the 2019 SSW event (Fig. 2). Geomagnetic activity can modulate the propagation of PWs and their interactions with tides, leading to temporal and spatial variations in the *Es* layers (Palo et al., 2005; Yamazaki et al., 2020). Therefore, even the weak disturbances that took place during the 2019 SSW may have contributed to some temporal differences and amplitude variations of the *ftEs* oscillations, further reinforcing the complexity of the interaction between atmospheric and ionospheric phenomena during SSW events.

Fig. 16 presents the wavelet power spectral analysis of the *ftEs* parameter for the period from August 21 to October 10, 2018, when no SSW event occurred in either the SH and NH. The analysis reveals that the BRI and DAR stations (SH in the Oceanian sector) did not exhibit oscillations characteristic of PWs. Similarly, no such oscillations were observed at the JEJ station (NH in the Asian sector). This absence of PW-related oscillations during non-SSW conditions strongly suggests that the long-period oscillations (~2–8-days) observed in the *ftEs* parameters during the 2019 SSW event (Figs. 5, 7, and 15, and Tables 4 and 6) are likely a result of non-linear interactions between tides and PWs. Furthermore, Fig. 16(a) and 16(b) show that at latitudes of the stations of BRI and DAR were dominated by diurnal tidal oscillations, while at JEJ station they exhibited diurnal, semidiurnal, and terdiurnal tidal oscillations.

4. Conclusions

In this study, we analyzed the effect of the rare Antarctic SSW event of 2019 on the top frequency parameter of the *Es* layers (*ftEs*), obtained from ionosonde measurements at low- and mid-latitude stations located across the American, Oceanian, and Asian continents. Additionally, we investigated the associated planetary wave (PW) oscillations, which were observed in the *Es* layers and atmospheric

winds at these stations. The main results of this study are summarized as follows:

1. The Antarctic SSW event of 2019 caused significant *ftEs* variations, with maximum peaks of ~20 MHz observed at comparatively lower-latitude stations in the South American and Oceanian sectors. At mid-latitudes stations in the American sector, the maximum *ftEs* peaks were between 12 and 17 MHz in the SH, while in the NH *ftEs* reached a maximum of 10–12 MHz. On the other hand, in the Oceanian and Asian continents, the maximum *ftEs* ranged from approximately 13 to 20 MHz. These atypical *ftEs* peaks, mainly those exceeding ~10 MHz, are consistent with previous studies, which have suggested that PW activity enhances electron density in the *Es* layers.
2. The wavelet analysis of *ftEs* revealed dominant diurnal and semidiurnal tidal oscillations, alongside secondary oscillations with periods of ~2–8-days. In the SH of the American continent, PW-induced oscillations were evident before and after the central day of the SSW event (DOY 260), showing periodicities of ~4–6-days. Similar patterns were observed in the SH of the Oceanian/Asian sector. In contrast, over the NH stations less intense PW oscillations have been observed, suggesting a weaker PW-tide interaction in these regions. Therefore, the 2–8-days periodicities observed in the *ftEs* parameter during the 2019 Antarctic SSW is attributed to the amplification of PWs and their non-linear interactions with the primary atmospheric tides. These interactions, favored by the unique conditions of the SSW, generated secondary waves that propagated into the lower thermosphere and modulated the wind shear responsible for *Es* layer formation. In contrast, such periodicity is absent during non-SSW periods, as demonstrated by our comparative analysis of the 2018 data (Fig. 16).
3. The analysis of zonal and meridional winds in the SH, particularly over the American continent, demonstrated that PW oscillations with periods of ~2–8-days were present before and after the central day of the SSW event. These results suggest a non-linear interaction between PWs and tides, likely driven by the increased global O_3 column and water vapor (H_2O), as well as the direct effects of the SSW event itself. The atmospheric coupling probably affected the electron density variability of the *Es* layers, as evidenced by the atypical *ftEs* peaks and secondary PW oscillations observed.
4. The results also suggest that the 2019 Antarctic SSW event caused significant interhemispheric impacts. The observed secondary PW oscillations in both hemispheres and their correlation with the enhancements in *ftEs* values, suggest a global-scale modulation of atmospheric dynamics. These findings agree with previous studies that have shown the interhemispheric propagation of disturbances during SSW events, further supporting the theory of enhanced troposphere-stratosphere-lower thermosphere coupling during such events.

Declaration of competing interest

The authors declare that they have no known competing financial interests or personal relationships that could have appeared to influence the work reported in this paper.

Acknowledgments

The authors thank the research support from the São Paulo Research Foundation (FAPESP, Brazil), Processes No. 2022/14815-5 and 2023/06293-1, the Conselho Nacional de Desenvolvimento Científico e Tecnológico (CNPq), grants nos. 314261/2020-6, 307519/2022-8, and 440882/2023-0, and the Coordenação de Aperfeiçoamento de Pessoal de Nível Superior (CAPES), grant no. 88887.924647/2023-00. EC also thanks the support from the Instituto Nacional de Pesquisas Espaciais/Ministry of Science, Technology and Innovation of Brazil (INPE/MCTI).

References

Andoh, S., Saito, A., Shinagawa, H., Ejiri, M.K., 2020. First simulations of day-to-day variability of mid-latitude sporadic E layer structures. Earth Planets Space 72 (165), 1–9. https://doi.org/10.1186/s40623-020-01299-8.

Andrioli, V.F., Xu, J., Batista, P.P., Resende, L.C.A., Da Silva, L.A., Marchezi, J.P., Li, H., Wang, C., Liu, Z., Guharay, A., 2022. New findings relating tidal variability and solar activity in the low latitude MLT region. J. Geophys. Res. Space Phys. 127, e2021JA030239. https://doi.org/10.1029/2021JA030239.

Andrioli, V.F., Clemesha, B.R., Batista, P.P., Schuch, N.J., 2009. Atmospheric tides and mean winds in the meteor region over Santa Maria (29.7°S; 53.8°W). J. Atmos. Sol. Terr. Phys. 71 (17–18), 1864–1876. https://doi.org/10.1016/j.jastp.2009.07.005.

Bergsson, B., Syndergaard, S., 2022. Global temporal and spatial variations of ionospheric sporadic-E derived from radio occultation measurements. J. Geophys. Res. Space Phys. 127, e2022JA030296. https://doi.org/10.1029/2022JA030296.

Buriti, R.A., Hocking, W.K., Batista, P.P., Medeiros, A.F., Clemesha, B. R., 2008. Observations of equatorial mesospheric winds over Cariri (7.4° S) by a meteor radar and comparison with existing models. Ann. Geophys. 26 (3), 485–497. https://doi.org/10.5194/angeo-26-485-2008.

Charlton, A.J., Polvani, L.M., 2007. A new look at stratospheric sudden warmings. Part I: climatology and modeling benchmarks. J. Clim. 20 (3), 449–469. https://doi.org/10.1175/JCLI3996.1.

Chau, J.L., Goncharenko, L.P., Fejer, B.G., Liu, H.-L., 2012. Equatorial and low latitude ionospheric effects during sudden stratospheric warming events. Space Sci. Rev. 168 (1–4), 385–417. https://doi.org/10.1007/s11214-011-9797-5.

Choi, H., Kim, B.-M., Choi, W., 2019. Type classification of sudden stratospheric warming based on pre- and postwarming periods. J. Clim. 32 (8), 2349–2367. https://doi.org/10.1175/JCLI-D-18-0223.1.

Chu, Y.H., Wang, C.Y., Wu, K.H., Chen, K.T., Tzeng, K.J., Su, C.L., Feng, W., Plane, J.M.C., 2014. Morphology of sporadic E layer retrieved from COSMIC GPS radio occultation measurements: wind shear theory examination. J. Geophys. Res. Space Phys. 119 (3), 2117–2136. https://doi.org/10.1002/2013JA019437.

Eswaraiah, S., Kim, J.H., Lee, W., Hwang, J., Kumar, K.N., Kim, Y.H., 2020. Unusual changes in the Antarctic middle atmosphere during the 2019 warming in the southern hemisphere. Geophys. Res. Lett. 47, e2020GL089199. https://doi.org/10.1029/2020GL089199.

Fagundes, P.R., Goncharenko, L.P., Abreu, A.J., Venkatesh, K., Pezzopane, M., Jesus, R., Gende, M., Coster, A.J., Pillat, V.G.,

2015. Ionospheric response to the 2009 sudden stratospheric warming over the equatorial, low, and middle latitudes in the South American sector. J. Geophys. Res. Space Phys. 120 (9), 7889–7902. https://doi.org/10.1002/2014JA020649.

Fontes, P.A., Muella, M.T.A.H., Resende, L.C.A., Jesus, R., Fagundes, P. R., Batista, P.P., Pillat, V.G., Tardelli, A., Andrioli, V.F., 2024. Effects of the northern hemisphere sudden stratospheric warmings on the sporadic-E layers in the Brazilian sector. J. Atmos. Sol. Terr. Phys. 256 (March), 106199–106214. https://doi.org/10.1016/j.jastp.2024.106199.

Fontes, P.A., Muella, M.T.A.H., Resende, L.C.A., Andrioli, V.F., Fagundes, P.R., Pillat, V.G., Batista, P.P., Carrasco, A.J., 2023. Effects of the terdiurnal tide on the sporadic E (Es) layer development at low latitudes over the Brazilian sector. Ann. Geophys. 41 (1), 209–224. https://doi.org/10.5194/angeo-41-209-2023.

Forbes, J.M., Zhang, X., Palo, S., Russell, J., Mertens, C.J., Mlynczak, M., 2008. Tidal variability in the ionospheric dynamo region. J. Geophys. Res. Space Phys. 113, A02310. https://doi.org/10.1029/2007JA012737.

Forbes, J.M., Zhang, X., 2015. Quasi-10-day wave in the atmosphere. J. Geophys. Res. Atmos. 120 (21), 11079–11089. https://doi.org/10.1002/2015JD023327.

Forbes, J.M., Zhang, X., 2017. The quasi-6 day wave and its interactions with solar tides. J. Geophys. Res. Space Phys. 122 (4), 4764–4776. https://doi.org/10.1002/2017JA023954.

Forbes, J.M., Zhang, X., Maute, A., 2020. Planetary wave (PW) generation in the thermosphere driven by the PW-modulated tidal spectrum. J. Geophys. Res. Space Phys. 125, e2019JA027704. https://doi.org/10.1029/2019JA027704.

Forbes, J.M., Wu, D., 2006. Solar tides as revealed by measurements of mesosphere temperature by the MLS experiment on UARS. J. Atmos. Sci. 63 (7), 1776–1797. https://doi.org/10.1175/JAS3724.1.

Gelaro, R., McCarty, W., Suárez, M.J., Todling, R., Molod, A., Takacs, L., Randles, C.A., Darmenov, A., Bosilovich, M.G., Reichle, R., et al., 2017. The modern-era retrospective analysis for research and applications, version 2 (MERRA-2). J. Clim. 30 (14), 5419–5454. https://doi.org/10.1175/JCLI-D-16-0758.1.

Giday, N.M., Katamzi, Z.T., McKinnell, L.-A., 2016. Ionospheric tomography over South Africa: comparison of MIDAS and ionosondes measurements. Adv. Space Res. 57 (1), 245–256. https://doi.org/10.1016/j.asr.2015.08.017.

Goncharenko, L.P., Coster, A.J., Plumb, R.A., Domeisen, D.I.V., 2012. The potential role of stratospheric ozone in the stratosphere-ionosphere coupling during stratospheric warmings. Geophys. Res. Lett. 39, L08101. https://doi.org/10.1029/2012GL051261.

Goncharenko, L.P., Harvey, V.L., Greer, K.R., Zhang, S.R., Coster, A.J., 2020. Longitudinally dependent low-latitude ionospheric disturbances linked to the Antarctic sudden stratospheric warming of September 2019. J. Geophys. Res. Space Phys. 125, e2020JA028199. https://doi.org/10.1029/2020JA028199.

Goncharenko, L.P., Harvey, V.L., Greer, K.R., Zhang, S.-R., Coster, A. J., Paxton, L.J., 2021. Impact of September 2019 Antarctic sudden stratospheric warming on mid-latitude ionosphere and thermosphere over North America and Europe. Geophys. Res. Lett. 48, e2021GL094517. https://doi.org/10.1029/2021GL094517.

Grinsted, A., Moore, J.C., Jevrejeva, S., 2004. Application of the cross wavelet transform and wavelet coherence to geophysical time series. Nonlinear Processes Geophys. 11 (5–6), 561–566. https://doi.org/10.5194/npg-11-561-2004.

Gu, S.-Y., Dou, X., Li, T., 2016. Influence of the Sudden stratospheric warming on quasi-2-day waves. Atmos. Chem. Phys. 16 (8), 4885–4896. https://doi.org/10.5194/acp-16-4885-2016.

Gu, S.-Y., Liu, H.-L., Dou, X., Jia, M., 2018. Ionospheric variability due to tides and quasi-two day wave interactions. J. Geophys. Res. Space Phys. 123 (2), 1554–1565. https://doi.org/10.1002/2017JA025105.

Hagan, M.E., Forbes, J.M., 2002. Migrating and nonmigrating diurnal tides in the middle and upper atmosphere excited by tropospheric latent heat release. J. Geophys. Res. Atmos. 107 (D24), 4754. https://doi.org/10.1029/2001JD001236.

Hagan, M.E., Forbes, J.M., 2003. Migrating and nonmigrating semidiurnal tides in the upper atmosphere excited by tropospheric latent heat release. J. Geophys. Res.: Space Phys. 108, 1062. https://doi.org/10.1029/2002JA009466.

Hagan, M.E., Maute, A., Roble, R.G., 2009. Tropospheric tidal effects on the middle and upper atmosphere. J. Geophys. Res. Space Phys. 114, A01302. https://doi.org/10.1029/2008JA013637.

Haldoupis, C., Pancheva, D., 2002. Planetary waves and midlatitude sporadic E layers: strong experimental evidence for a close relationship. J. Geophys. Res. 107 (A6), SIA 3-1–SIA 3-6. https://doi.org/10.1029/2001JA000212.

Haldoupis, C., Pancheva, D., Singer, W., Meek, C., MacDougall, J., 2007. An explanation for the seasonal dependence of midlatitude sporadic E layers. J. Geophys. Res. Space Phys. 112, A06315. https://doi.org/10.1029/2007JA012322.

Haldoupis, C., Pancheva, D., 2006. Terdiurnal Tidelike variability in sporadic E layers. J. Geophys. Res. Space Phys. 111, A07303. https://doi.org/10.1029/2005JA011522.

Haldoupis, C., Pancheva, D., Mitchell, N.J., 2004. A study of tidal and planetary wave periodicities present in midlatitude sporadic E layers. J. Geophys. Res. Space Phys. 109, A02302. https://doi.org/10.1029/2003JA010253.

Hocking, W.K., 2004. Radar meteor decay rate variability and atmospheric consequences. Ann. Geophys. 22 (11), 3805–3818. https://doi.org/10.5194/angeo-22-3805-2004.

Huang, J., MacDougall, J.W., 2005. Legendre coding for digital ionosondes. Radio Sci. 40, RS4013. https://doi.org/10.1029/2004RS003123.

Jesus, R., Batista, I.S., Jonah, O.F., Abreu, A.J., Fagundes, P.R., Venkatesh, K., Denardini, C.M., 2017. An investigation of the ionospheric disturbances due to the 2014 sudden stratospheric warming events over Brazilian sector. J. Geophys. Res. Space Phys. 122 (11), 11698–11715. https://doi.org/10.1002/2017JA024560.

Korenkov, Y.N., Klimenko, V.V., Klimenko, M.V., Bessarab, F.S., Korenkova, N.A., Ratovsky, K.G., Chernigovskaya, M.A., Shcherbakov, A.A., Sahai, Y., Fagundes, P.R., Jesus, R., Abreu, A.J., Condor, P., 2012. The global thermospheric and ionospheric response to the 2008 minor sudden stratospheric warming event. J. Geophys. Res. Space Phys. 117, A10309. https://doi.org/10.1029/2012JA018018.

Korenkova, N.A., Leschenko, V.S., Cherniak, I.V., Korenkov, Y.N., 2015. Coupling between parameters of Es layer and planetary waves during SSW 2008, 2010. Adv. Space Res. 56 (9), 1886–1894. https://doi.org/10.1016/j.asr.2015.07.031.

Krüger, K., Naujokat, B., Labitzke, K., 2005. The unusual midwinter warming in the southern hemisphere stratosphere 2002: a comparison to northern hemisphere phenomena. J. Atmos. Sci. 62 (3), 603–613. https://doi.org/10.1175/JAS-3316.1.

Li, N., Luan, X., Lei, J., Bolaji, O.S., Owolabi, C., Chen, J., Xu, Z., Li, G., Ning, B., 2020. Variations of mesospheric neutral winds and tides observed by a meteor radar chain over China during the 2013 sudden stratospheric warming. J. Geophys. Res. Space Phys. 125, e2019JA027443. https://doi.org/10.1029/2019JA027443.

Lilienthal, F., Jacobi, C., Geißler, C., 2018. Forcing mechanisms of the terdiurnal tide. Atmos. Chem. Phys. 18 (21), 15725–15742. https://doi.org/10.5194/acp-18-15725-2018.

Lima, L.M., Alves, E.O., Batista, P.P., Clemesha, B.R., Medeiros, A.F., Buriti, R.A., 2012. Sudden stratospheric warming effects on the mesospheric tides and 2-day wave dynamics at 7°S. J. Atmos. Solar-Terrestrial Phys. 79 (April), 99–107. https://doi.org/10.1016/j.jastp.2011.02.013.

Limpasuvan, V., Orsolini, Y.J., Chandran, A., Garcia, R.R., Smith, A.K., 2016. On the composite response of the MLT to major sudden stratospheric warming events with elevated stratopause. J. Geophys. Res. Atmos. 121 (9), 4518–4537. https://doi.org/10.1002/2015JD024401.

Lin, J.T., Lin, C.H., Rajesh, P.K., Yue, J., Lin, C.Y., Matsuo, T., 2020. Local-time and vertical characteristics of quasi-6-day oscillation in the ionosphere during the 2019 Antarctic sudden stratospheric warming.

Geophys. Res. Lett. 47, e2020GL090345. https://doi.org/10.1029/2020GL090345.

Liu, G., Hirooka, T., Eguchi, N., Krüger, K., 2022. Dynamical evolution of a minor sudden stratospheric warming in the southern hemisphere in 2019. Atmos. Chem. Phys. 22 (5), 3493–3505. https://doi.org/10.5194/acp-22-3493-2022.

Luo, J., Ma, Z., Gong, Y., Zhang, S., Xiao, Q., Huang, C., Huang, K., 2023. Record-strong eastward propagating 4-day wave in the southern hemisphere observed during the 2019 Antarctic sudden stratospheric warming. Geophys. Res. Lett. 50, e2022GL102704. https://doi.org/10.1029/2022GL102704.

Ma, Z., Gong, Y., Zhang, S.D., Luo, J.H., Zhou, Q.H., Huang, C.M., Huang, K.M., 2020. Comparison of stratospheric evolution during the major sudden stratospheric warming events in 2018 and 2019. Earth Planet. Phys. 4 (5), 1–11. https://doi.org/10.26464/epp2020044.

Ma, Z., Gong, Y., Zhang, S., Xiao, Q., Xue, J., Huang, C., Huang, K., 2022. Understanding the excitation of quasi-6-day waves in both hemispheres during the September 2019 Antarctic SSW. J. Geophys. Res.: Atmos. 127, e2021JD035984. https://doi.org/10.1029/2021JD035984.

Maksyutin, S.V., Sherstyukov, O.N., 2005. Dependence of E-sporadic layer response on solar and geomagnetic activity variations from its ion composition. Adv. Space Res. 35 (8), 1496–1499. https://doi.org/10.1016/j.asr.2005.05.062.

Maksyutin, S.V., Sherstyukov, O.N., Fahrutdinova, A.N., 2001. Dependence of sporadic-E layer and lower thermosphere dynamics on solar activity. Adv. Space Res. 27 (6–7), 1265–1270. https://doi.org/10.1016/S0273-1177(01)00195-8.

Mathews, J.D., 1998. Sporadic E: current views and recent progress. J. Atmos. Sol. Terr. Phys. 60 (4), 413–435. https://doi.org/10.1016/S1364-6826(97)00043-6.

Matsuno, T., 1971. A dynamical model of the stratospheric sudden warming. J. Atmos. Sci. 28 (8), 1479–1494. https://doi.org/10.1175/1520-0469(1971)028<1479:ADMOTS>2.0.CO;2.

Matzka, J., Stolle, C., Yamazaki, Y., Bronkalla, O., Morschhauser, A., 2021. The geomagnetic Kp index and derived indices of geomagnetic activity. Space Weather 19, e2020SW002641. https://doi.org/10.1029/2020SW002641.

Mitra, G., Guharay, A., 2024. Impact of sudden stratospheric warming on middle atmospheric circulation in the southern hemisphere: a comparative study. J. Atmos. Sol. Terr. Phys. 254 (January), 106173–106186. https://doi.org/10.1016/j.jastp.2024.106173.

Mitra, G., Guharay, A., Batista, P.P., Buriti, R.A., 2022. Impact of the September 2019 minor sudden stratospheric warming on the low-latitude middle atmospheric planetary wave dynamics. J. Geophys. Res. Atmos. 127, e2021JD035538. https://doi.org/10.1029/2021JD035538.

Mitra, G., Guharay, A., Batista, P.P., Buriti, R.A., Moffat-Griffin, T., 2023. Investigation on the MLT tidal variability during September 2019 minor sudden stratospheric warming. Adv. Space Res. 71 (1), 869–882. https://doi.org/10.1016/j.asr.2022.08.017.

Miyoshi, Y., Yamazaki, Y., 2020. Excitation mechanism of ionospheric 6-day oscillation during the 2019 September sudden stratospheric warming event. J. Geophys. Res. Space Phys. 125, e2020JA028283. https://doi.org/10.1029/2020JA028283.

Mo, X., Zhang, D., 2020. Quasi-10 d wave modulation of an equatorial ionization anomaly during the southern hemisphere stratospheric warming of 2002. Annales Geophysicae 38 (1), 9–16. https://doi.org/10.5194/angeo-38-9-2020.

Moudden, Y., Forbes, J.M., 2013. A decade-long climatology of terdiurnal tides using TIMED/SABER observations. J. Geophys. Res. Space Phys. 118 (7), 4534–4550. https://doi.org/10.1002/jgra.50273.

Noguchi, S., Kuroda, Y., Kodera, K., Watanabe, S., 2020. Robust enhancement of tropical convective activity by the 2019 antarctic sudden stratospheric warming. Geophys. Res. Lett. 47, e2020GL088743. https://doi.org/10.1029/2020GL088743.

Oberheide, J., Forbes, J.M., Zhang, X., Bruinsma, S.L., 2011. Climatology of upward propagating diurnal and semidiurnal tides in the thermosphere. J. Geophys. Res. Space Phys. 116, A11306. https://doi.org/10.1029/2011JA016784.

Palo, S.E., Forbes, J.M., Zhang, X., Russell, J.M., Mertens, C.J., Mlynczak, M.G., Burns, G.B., Espy, P.J., Kawahara, T.D., 2005. Planetary wave coupling from the stratosphere to the thermosphere during the 2002 southern hemisphere pre-stratwarm period. Geophys. Res. Lett. 32, L23809. https://doi.org/10.1029/2005GL024298.

Pancheva, D., Haldoupis, C., Meek, C.E., Manson, A.H., Mitchell, N.J., 2003. Evidence of a role for modulated atmospheric tides in the dependence of sporadic e layers on planetary waves. J. Geophys. Res. Space Phys. 108 (A5), 1176. https://doi.org/10.1029/2002JA009788.

Pancheva, D., Mukhtarov, P., Andonov, B., Mitchell, N.J., Forbes, J.M., 2009. Planetary waves observed by TIMED/SABER in coupling the stratosphere–mesosphere–lower thermosphere during the winter of 2003/2004: Part 1—comparison with the UKMO temperature results. J. Atmos. Sol. Terr. Phys. 71 (1), 61–74. https://doi.org/10.1016/j.jastp.2008.09.016.

Pillat, V.G., Guimarães, L.N.F., Fagundes, P.R., Silva, J.D.S., 2013. A computational tool for ionosonde CADI's ionogram analysis. Comput. Geosci. 52 (March), 372–378. https://doi.org/10.1016/j.cageo.2012.11.009.

Rao, J., Garfinkel, C.I., White, I.P., Schwartz, C., 2020. The southern hemisphere minor sudden stratospheric warming in September 2019 and its predictions in S2S models. J. Geophys. Res. Atmos. 125, e2020JD032723. https://doi.org/10.1029/2020JD032723.

Rao, J., Ren, R., 2020. Modeling study of the destructive interference between the tropical Indian ocean and eastern pacific in their forcing in the southern winter extratropical stratosphere during ENSO. Climate Dyn. 54 (3–4), 2249–2266. https://doi.org/10.1007/s00382-019-05111-6.

Rao, J., Ren, R., Chen, H., Yu, Y., Zhou, Y., 2018. The stratospheric sudden warming event in February 2018 and its prediction by a climate system model. J. Geophys. Res. Atmos. 123 (23), 13332–13345. https://doi.org/10.1029/2018JD028908.

Reinisch, B.W., Galkin, I.A., Khmyrov, G.M., Kozlov, A.V., Bibl, K., Lisysyan, I.A., Cheney, G.P., Huang, X., Kitrosser, D.F., Paznukhov, V.V., Luo, Y., Jones, W., Stelmash, S., Hamel, R., Grochmal, J., 2009. New digisonde for research and monitoring applications. Radio Sci. 44, RS0A24. https://doi.org/10.1029/2008RS004115.

Ren, R.-C., Cai, M., 2008. Meridional and downward propagation of atmospheric circulation anomalies. Part II: southern hemisphere cold season variability. J. Atmos. Sci. 65 (7), 2343–2359. https://doi.org/10.1175/2007JAS2594.1.

Resende, L.C.A., Arras, C., Batista, I.S., Denardini, C.M., Bertollotto, T. O., Moro, J., 2018. Study of sporadic e layers based on GPS radio occultation measurements and Digisonde data over the Brazilian region. Ann. Geophys. 36 (2), 587–593. https://doi.org/10.5194/angeo-36-587-2018.

Roy, R., Kuttippurath, J., Lefèvre, F., Raj, S., Kumar, P., 2022. The sudden stratospheric warming and chemical ozone loss in the Antarctic winter 2019: comparison with the winters of 1988 and 2002. Theor. Appl. Climatol. 149 (1–2), 119–130. https://doi.org/10.1007/s00704-022-04031-6.

Safieddine, S., Bouillon, M., Paracho, A.C., Jumelet, J., Tencé, F., Pazmino, A., Goutail, F., Wespes, W., Bekki, S., Boynard, A., Hadji-Lazaro, J., Coheur, P.-F., Hurtmans, D., Clerbaux, C., 2020. Antarctic ozone enhancement during the 2019 sudden stratospheric warming event. Geophys. Res. Lett. 47, e2020GL087810. https://doi.org/10.1029/2020GL087810.

Shalimov, S., Haldoupis, C., 2002. A model of mid-latitude E-region plasma convergence inside a planetary wave cyclonic vortex. Ann. Geophys. 20 (8), 1193–1201. https://doi.org/10.5194/angeo-20-1193-2002.

Shalimov, S., Haldoupis, C., Voiculescu, M., Schlegel, K., 1999. Midlatitude E region plasma accumulation driven by planetary wave horizontal wind shears. J. Geophys. Res. Space Phys. 104 (A12), 28207–28213. https://doi.org/10.1029/1999JA900316.

Shen, X., Wang, L., Osprey, S., 2020. The southern hemisphere sudden stratospheric warming of September 2019. Sci. Bull. 65 (21), 1800–1802. https://doi.org/10.1016/j.scib.2020.06.028.

Siddiqui, T.A., Maute, A., Pedatella, N.M., 2019. On the importance of interactive ozone chemistry in earth-system models for studying mesosphere-lower thermosphere tidal changes during sudden stratospheric warmings. J. Geophys. Res. Space Phys. 124 (12), 10690–10707. https://doi.org/10.1029/2019JA027193.

Statnaia, I.A., Karpechko, A.Y., Järvinen, H.J., 2020. Mechanisms and Predictability of Sudden Stratospheric Warming in Winter 2018. Weather Clim. Dyn. 1 (2), 657–674. https://doi.org/10.5194/wcd-1-657-2020.

Tang, Q., Zhou, C., Liu, H., Du, Z., Liu, Y., Zhao, J., Yu, Z., Zhao, Z., Feng, X., 2022. Global structure and seasonal variations of the tidal amplitude in sporadic-E layer. J. Geophys. Res. Space Phys. 127, e2022JA030711. https://doi.org/10.1029/2022JA030711.

Teitelbaum, H., Vial, F., 1991. On tidal variability induced by nonlinear interaction with planetary waves. J. Geophys. Res. Space Phys. 96 (A8), 14169–14178. https://doi.org/10.1029/91JA01019.

Veenus, V., Das, S.S., 2024. Role of southern hemisphere sudden stratospheric warming in altering the intensity of Brewer-Dobson circulation and its impact on stratospheric ozone and water vapor. Adv. Space Res. 73 (5), 2598–2608. https://doi.org/10.1016/j.asr.2023.12.012.

Veenus, V., Das, S.S., Liji, M.D., 2023. Ozone changes due to sudden stratospheric warming-induced variations in the intensity of Brewer-Dobson circulation: a composite analysis using observations and chemical-transport model. Geophys. Res. Lett. 50, e2023GL103353. https://doi.org/10.1029/2023GL103353.

Voiculescu, M., Haldoupis, C., Pancheva, D., Ignat, M., Schlegel, K., Shalimov, S., 2000. More evidence for a planetary wave link with midlatitude E region coherent backscatter and sporadic E layers. Ann. Geophys. 18 (9), 1182–1196. https://doi.org/10.1007/s005850000261.

Wang, H., Fuller-Rowell, T.J., Akmaev, R.A., Hu, M., Kleist, D.T., Iredell, M.D., 2011. First simulations with a whole atmosphere data assimilation and forecast system: the January 2009 major sudden stratospheric warming. J. Geophys. Res. Space Phys. 116, A12321. https://doi.org/10.1029/2011JA017081.

Whitehead, J.D., 1989. Recent work on mid-latitude and equatorial sporadic-E. J. Atmos. Terrestrial Phys. 51 (5), 401–424. https://doi.org/10.1016/0021-9169(89)90122-0.

Xie, J., Hu, J., Xu, H., Liu, S., He, H., 2020. Dynamic Diagnosis of stratospheric sudden warming event in the boreal winter of 2018 and its possible impact on weather over North America. Atmosphere 11 (5), 438. https://doi.org/10.3390/atmos11050438.

Yamazaki, Y., Matthias, V., Miyoshi, Y., Stolle, C., Siddiqui, T., Kervalishvili, G., Laštovička, J., Kozubek, M., Ward, W., Themens, D.R., Kristoffersen, S., Alken, P., 2020. September 2019 Antarctic sudden stratospheric warming: quasi-6-day wave burst and ionospheric effects. Geophys. Res. Lett. 47, e2019GL086577. https://doi.org/10.1029/2019GL086577.

Yu, B., Xue, X., Scott, C.J., Wu, J., Yue, X., Feng, W., Chi, Y., Marsh, D. R., Liu, H., Dou, X., Plane, J.M.C., 2021. Interhemispheric transport of metallic ions within ionospheric sporadic E layers by the lower thermospheric meridional circulation. Atmos. Chem. Phys. 21 (5), 4219–4230. https://doi.org/10.5194/acp-21-4219-2021.

Zhang, J., Limpasuvan, V., Orsolini, Y.J., Espy, P.J., Hibbins, R.E., 2021. Climatological westward-propagating semidiurnal tides and their composite response to sudden stratospheric warmings in SuperDARN and SD-WACCM-X. J. Geophys. Res. Atmos. 126, e2020JD032895. https://doi.org/10.1029/2020JD032895.

Zhang, X., Forbes, J.M., Hagan, M.E., 2010a. Longitudinal variation of tides in the MLT region: 1. Tides driven by tropospheric net radiative heating. J. Geophys. Res. Space Phys. 115, A06316. https://doi.org/10.1029/2009JA014897.

Zhang, X., Forbes, J.M., Hagan, M.E., 2010b. Longitudinal variation of tides in the MLT region: 2. Relative effects of solar radiative and latent heating. J. Geophys. Res. Space Phys. 115, A06317. https://doi.org/10.1029/2009JA014898.